Spring 2023

Characterization of Bistability Behavior in Unsymmetric CFRP Laminates

Evan Medora
Embry-Riddle Aeronautical University, medorae@my.erau.edu

Scholarly Commons Citation
Medora, Evan, "Characterization of Bistability Behavior in Unsymmetric CFRP Laminates" (2023). *Doctoral Dissertations and Master's Theses*. 748.
https://commons.erau.edu/edt/748

CHARACTERIZATION OF BISTABILITY BEHAVIOR IN UNSYMMETRIC CFRP LAMINATES

By

Evan Medora

A Thesis Submitted to the Faculty of Embry-Riddle Aeronautical University

In Partial Fulfillment of the Requirements for the Degree of

Master of Science in Aerospace Engineering

April 2023

Embry-Riddle Aeronautical University

Daytona Beach, Florida

CHARACTERIZATION OF BISTABILITY BEHAVIOR IN UNSYMMETRIC CFRP LAMINATES

By

Evan Medora

This Thesis was prepared under the direction of the candidate's Thesis Committee Chair, Dr. Sirish Namilae, Department of Aerospace Engineering, and has been approved by the members of the Thesis Committee. It was submitted to the Office of the Senior Vice President for Academic Affairs and Provost, and was accepted in the partial fulfillment of the requirements for the Degree of Master of Science in Aerospace Engineering.

THESIS COMMITTEE

Chair, Dr. Sirish Namilae	Member, Dr. David Sypeck
Member, Dr. Fady Barsoum	
Graduate Program Coordinator, Dr. Hever Moncayo	Date
Dean of the College of Engineering, Dr. James W. Gregory	Date
Associate Provost of Academic Support, Dr. Christopher Grant	Date

ACKNOWLEDGEMENTS

I would like to extend my gratitude to my committee chair and advisor, Dr. Sirish Namilae. Your mentorship and support are invaluable. I would also like to thank my committee members, Dr. Fady Barsoum and Dr. David Sypeck, for their access to equipment, advice, and for showing interest in this research. Thank you to all of the students who have assisted my research in the Composites and associated labs; working along side such brilliant people is a joy.

Finally, thank you to my university and the U.S. Department of Education for the Graduate Assistance in Areas of National Need (GAANN) fellowship. Your financial support has gone a long way to support me and this study.

ABSTRACT

Composite laminates of unsymmetric layup families often exhibit twin stable shapes at room temperature, a phenomenon known as bistability. Unsymmetric bistable composite laminates have often been suggested for applications in aerospace morphing structures, damping, and energy storage, because of their ability to easily change their shape while being homogenized with the rest of the composite structure.

This study analyzes the mechanisms responsible for bistability in unsymmetrical [0/0/90/90] laminates through a combination of experiments and modeling. Several unsymmetrical laminates with different aspect ratios were fabricated using autoclave processing. Digital image correlation (DIC) is used to monitor laminate strains in situ during the processing of the composite and to correlate processing strains to the degree of bistable behavior in differently sized samples. Room-temperature curvatures were measured and compared with analytical and FEA models. Load responses to changes in the shape of the laminate were measured for each sample size to determine the effects of the size and aspect ratio for both as-fabricated and machined samples. It is shown that the “snap-through” load and curvatures of the laminates decrease as the length of one side of the sample decreases. It is also shown that the snap-through load of samples further machined with a water jet cutter post-cure decreased significantly, but possessed only slightly less curvature compared to identically sized samples that were not machined. The results show that there are significant limitations to the application of this type of laminate, but there is ample potential for property modification during processing, which can increase the size of the design space.

TABLE OF CONTENTS

ACKNOWLEDGEMENTS .... **i**

ABSTRACT .... **ii**

TABLE OF CONTENTS .... **iii**

LIST OF FIGURES .... **v**

LIST OF TABLES .... **viii**

LIST OF ACRONYMS .... **ix**

LIST OF SYMBOLS .... **x**

1 Introduction **1**

1.1 Motivation 2

1.2 Objectives 3

2 Review of Relevant Literature **4**

2.1 Aerospace Composites 4

2.2 Applications for Bistable Composites 5

2.3 Bistability Fundamentals 7

2.4 Computational and Analytical Work 10

2.5 Recent Research 10

3 Experimental Methodology **13**

3.1 Materials 13

3.2 Autoclave Processing DIC Analysis 14

3.3 Snap-Through Load Testing 29

3.4 Post Cure Machining... 33

4 Analytical and Computational Methods 37

4.1 Analytical Model 37

4.2 Finite Element Model 40

5 Results 43

5.1 Digital Image Correlation Method for In-Situ Strain Results.................................. 43

5.2 Curvature Measurements of Cured Samples Results.. 46

5.3 Effects of Post-Cure Machining.. 47

5.4 Effects of Cure Cycle Modification.. 50

5.5 Analytical Model 51

5.6 ANSYS Cure Simulation 52

6.1 Comparison of Results from Literature 54

6.2 Discussion on the Analytical Model 55

7 Conclusions and Future Work 56

7.1 Future Work 56

9 APPENDIX A: Hyer Model Code, MATLAB 60

LIST OF FIGURES

Figure **Page**

Figure 1.1 Artist concept of a vehicle with morphing wing. [1].. 1

Figure 2.1 Design for wing spars with a bistable morphing section for variable sweep. [5]. . 7

Figure 2.2 Different configurations of tessellated bistable laminates that show the multitude of potential shapes when combining different layups. [15] 11

Figure 3.1 View of ASC Econoclave 2x4 with viewports and controlling Dell (Round Rock, TX) PC.. 14

Figure 3.2 Close up of viewport and Correlated Solutions DIC cameras............................. 15

Figure 3.3 Schematic diagram of camera Field of View (FOV) on CFRP sample within autoclave. The camera angle and sample position were adjusted until the minimum amount of glare was achieved... 16

Figure 3.4 Selected equipment and materials. Note the calibration tile in the upper center of the image. The specific spacing and pattern of the dots on this tile allow the cameras to have a base for their analysis. 17

Figure 3.5 Exploded view of a sample ready to be placed in an autoclave.. 18

Figure 3.6 Top view of a 152.4 cm square autoclave sample with a speckle pattern for DIC. 19

Figure 3.7 Sample setup within autoclave, viewport opening can be seen in upper right. Make sure to use two vacuum probes, one for vacuum source, and the other for vacuum probe.... 20

Figure 3.8 Normal “dwell and cure” cure cycle. The recipe for the autoclave consisted of five steps. a: Initial heating from room temperature at 5°C/min. b: 30 min “dwell” period at 80°C to reduce wrinkling and improve DIC accuracy. c: 2°C/min heating to curing temperature of 130 °C. d: 120-min cure period. e: Unlimited cooling rate phase to bring the sample to 50°C for removal from the autoclave. 22

Figure 3.9 Interrupted cure cycle (red) compared with the normal cure cycle...................... 23

Figure 3.10 View of common flaws that affect DIC accuracy in laminate normal strain in the direction of the x-axis (e_{xx}) strain contour plots. Top left: A zone of poor-quality speckles, uncolored because the DIC software was unable to analyze them in the contour plot of the sample. Top right: Band of glare, wrinkle in vacuum bagging, and resin bubbles. Note the increased glare of the wrinkles. Bottom left: Effect of wrinkles and bubbles on DIC analysis, causing holes in the contour plot. Bottom right: DIC contour plot of fair quality with a good speckle pattern and no bubbles, only interrupted by a wrinkle.. 26

Figure 3.11 Diagram showing the four measurements needed to find the laminate curvatures in both stable shapes. 27

Figure 3.12 Range of samples cured in autoclave. 29

Figure 3.13 Experiment diagram of snap-through testing. All edges of the laminate are free. 31

Figure 3.14 Image of the force tester setup with laminate before being snapped through.... 32

Figure 3.15 Plot of the load response for the snap-through load tests. It can be seen that the square 15.24cm x 15.24cm sample (black) carries more residual stress than the 15.24cm x 10.16cm sample (red), which means more force is required to change the shape of the larger sample. 33

Figure 3.16 OMAX Maxiem 1515 water jet cutter of the kind used to cut samples. [21] 35

Figure 3.17 Water jet cutter in operation, next to laminate sample taped to tool plate. It is necessary to make sure the laminate is as flat as possible for this process................................. 36

Figure 4.1 Types of room temperature laminate shapes predicted by Hyer's model. (a): *a* constant is positive and *b* constant is negative. (b): $a > 0$ and $b = 0$. (c): $a = 0$ and $b < 0$........... 38

Figure 4.2 Flowchart figure of the analytical model... 40

Figure 4.3 Function responsible for determining the A, B and D matrices and thermal forces and moments. 39

Figure 4.4 The series of functions in MATLAB code. a(i) represents the constants *a* and *b*.. 40

Figure 4.5 The MATLAB code that solves the equations for the constants.......................... 40

Figure 5.1 e_{xx} strains for 15.24 cm x 15.24 cm $[0_2/90_2]$ sample, ID 663. This is approximately 5 min into the cure cycle, and it can be seen from the random pattern and low strain magnitudes that almost no strain has yet developed in the laminate. Pictured area is approximately 6cm by 5cm.. 44

Figure 5.2 The e_{xx} strains for the same sample approximately 25 min into the curing cycle. On average, over the surface, a net positive e_{xx} strain is formed as its magnitude increases owing to thermal conditions... 44

Figure 5.3 e_{xx} strains around 2h into the cure, when the strain increase reached its peak and the contour plot became almost uniformly positive. 45

Figure 5.4 e_{xx} residual strains for multiple sizes of $[0_2/90_2]$ samples 46

Figure 5.5 AR vs. curvature for $[0_2/90_2]$ samples. The side that is 15.24 cm [6 in] for all samples stays mostly constant in curvature, unaffected by the decrease in length of the other side.. 47

Figure 5.6 AR vs. snap-through load for machined and non-machined $[0_2/90_2]$ samples. 49

Figure 5.7 AR vs. curvature for the side of changing length for machined and non-machined $[0_2/90_2]$ samples. 49

Figure 5.8 e_{xx} residual strains for $[0_2/90_2]$ 15.24×15.24 cm [6x6 in] samples with and without cure interruption. 51

Figure 5.9 AR vs. curvature for the side of changing length forthe experimental $[0_2/90_2]$ samples and from the analytical model. 52

Figure 5.10 AR vs. curvature for the side of changing length from the ANSYS FEA model. 53

Figure 5.11 Saddle shaped laminate in ANSYS. 53

Figure 6.1 Experimental curvature results for the shortening side compared to the version of the analytical model where only solutions where b=0 are allowed, and the model without that restriction. 55

LIST OF TABLES

Table **Page**

Table 2.1 Important events in the history of aerospace composite usage. [3]. 5

Table 3.1 List of material properties for the CFRP prepreg in this study............................. 13

Table 3.2 List of samples produced for research. Samples labeled “Water Jet Cutter” were machined down from originally being 15.24cm x 15.24cm samples, to 15.24cm x 10.16cm, and then to 15.24cm x 7.62cm. 28

Table 4.1 List of material properties used by ACCS to model the material used for FEA study. 42

LIST OF ACRONYMS

CFRP	Carbon Fiber Reinforced Polymer
DIC	Digital Image Correlation
FE/FEA	Finite Element Analysis
AR	Aspect Ratio
FOV	Field of View
CLT	Classical Laminate Theory
ACP	ANSYS Composite PrepPost
ACCS	ANSYS Composite Cure Simulator

LIST OF SYMBOLS

θ	Laminate angle
h	Height of laminate curvature
L	Laminate side length
R	Laminate radius of curvature
κ	Laminate curvature
E	Young's modulus
v	Poisson's ratio
w	Laminate z-axis displacement
a_i/b_i	Displacement field constants
ε_x^0	In plane strain, x direction
ε_y^0	In plane strain, y direction
ε_{xy}^0	In plane shear strain
W	Laminate potential energy
V	Laminate volume
ω	Laminate strain energy density
e_{xx}	Laminate normal strain in the direction of the x-axis
F	Applied force
t	Laminate thickness

1 Introduction

Advancements in material technologies have always been a great boon for vehicle design in the aerospace industry. Novel methods of using materials in vehicle design, from the advent of the first metallic semi-monocoque aircraft to the beginning of composite structures in aircraft and spacecraft, have allowed designers to take significant steps to improve vehicle performance and have facilitated new designs that would have been impossible to fabricate previously. One such design area that is being researched heavily is "morphing" aerospace structures, which refers to structures that can smoothly alter their shape to permit a high degree of aerodynamic performance, control, and efficiency. However, with new revolutionary materials and ways to use them, there are always obstacles to overcome and questions that need to be answered on the path from theory and research to application and industry.

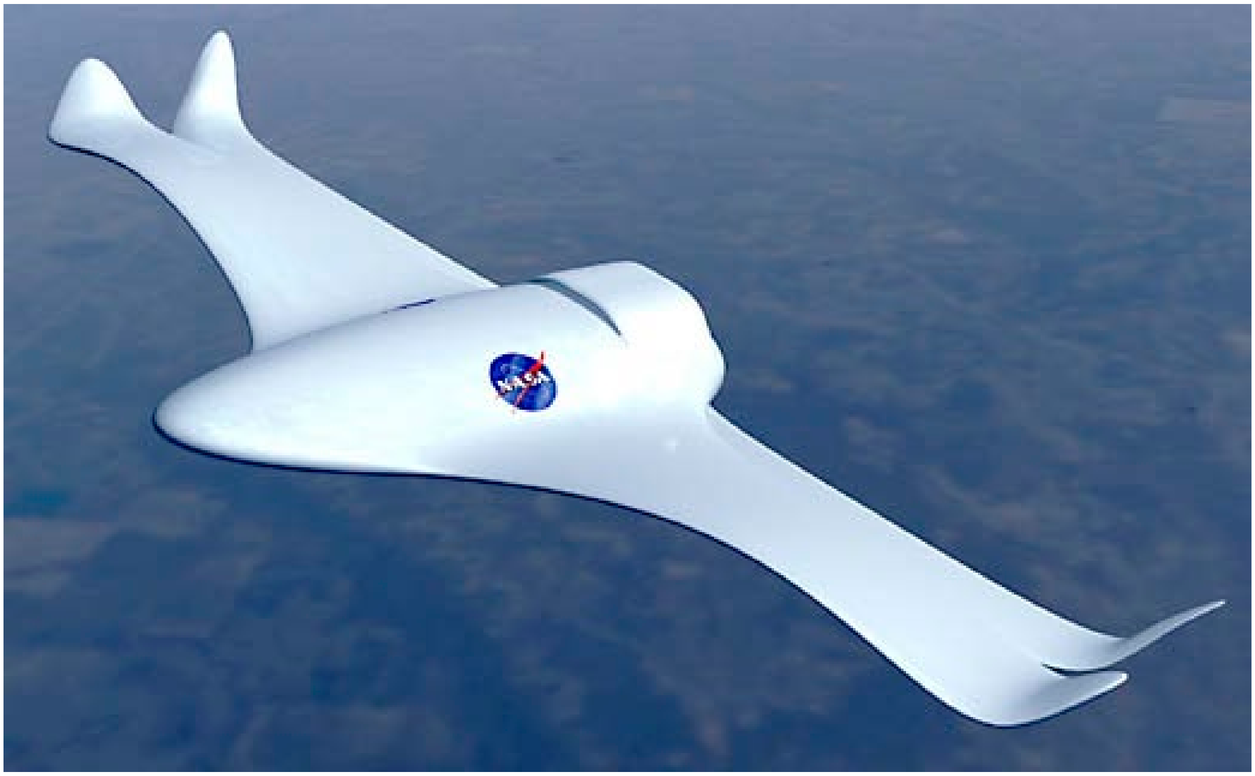

Figure 1.1 Artist concept of a vehicle with morphing wing. [1]

1.1 Motivation

Despite early studies by Hyer [2] during the 1980s, bistable composite laminates are still on the path for application in aerospace vehicle design (as well as other fields where these types of structures could be useful). This is not due to a lack of research, as there is a large body of research on the properties and applications of this type of laminate structure. It hints at the level of complexity and several almost unavoidable pitfalls when considering utilizing bistable laminates in an aerospace morphing structure application. This one of the most promising of all applications considered by the body of research reviewed in this paper. Unsymmetric bistable laminates are a good fit for morphing structures that can be blended into traditional types of carbon fiber-reinforced polymer (CFRP) aerospace structures because of the large amount of deflection that can be gained from very little force input, as well as the fact that both equilibrium shapes of the laminate are stable, and thus no force input is required to keep them in the desired shapes. It is also possible to seamlessly create an unsymmetric bistable section in a CFRP structure by simply modifying the layup of the structure locally, which can be achieved using several methods. However, an often-overlooked limitation of the bistable behavior of this type of laminate is its edge length/aspect ratio and thickness of the laminate. This means that in some cases, although a small component or a high-thickness component would be most efficient for an application, the component will lack the desired bistability behavior and will not be able to be used. In short, the application of bistable laminates to a morphing structure design quickly becomes a difficult balancing act of the intertwined parameters of desired curvature, laminate size and thickness, allowable actuation load, and stiffness of the structure. The problem quickly develops into a "Goldilocks zone" type restriction, where a structure must not be too large or too small unless large sacrifices are made elsewhere. From the applications done in research, this zone seems to be somewhere around structures that would be commonly found on a medium sized UAV. Combining this with other requirements, a vehicle or structure must satisfy, and the application of bistable morphing structures can, in many cases, be unfeasible.

1.2 Objectives

The objective of this thesis is to refine any prospective designer's understanding of bistable CFRP laminates so that they are aware of the obstacles they face in the design process. In addition, this study introduces a range of helpful tools to characterize and modify the properties of a given bistable laminate structure, which would specifically aid in designing aerospace morphing structures that incorporate bistable laminates. First, this study investigates the main factors that affect the bistability behavior in CFRP laminates, namely laminate geometry (side length and aspect ratio), the cure profile of the laminate, and the effects of post-cure machining. A range of 4-ply unsymmetric CFRP samples were produced with different aspect ratios, and alternate cure profiles were used for some samples. Subsequently, large samples were machined using a water jet cutter to change the side length and compared to laminates cured as plates of identical size. Second, the development of bistability during composite processing was studied in-situ using Digital Image Correlation (DIC). These two objectives serve as the basis for the third objective: to study how the snap-through load, the force required to change the shape of the laminate from one stable state to the other, of bistable laminates can be modified to a designer's specifications during and after the initial processing of the laminate. The goal of the objectives is clear: by increasing the number of ways we can modify the properties of bistable laminates, and by allowing greater modification of the laminates, the design space for applications will widen, allowing more leeway for morphing structures using bistable laminates to be implemented in vehicle design.

2 Review of Relevant Literature

Bistable laminates is the name given to any type of composite laminate that has two stable shapes and can switch, or “snap” (a name given due to the sound that is usually made by the laminate) between these two states when a force or moment is applied. Although laminates that develop curvature after curing are usually considered unfeasible for use, the ability to swap between two shapes can be advantageous. One easily visualized example, although metallic, is most tape-measures. Tape measures use the same basic premise of bistability as that of bistable laminates. Many feet of the tape measure can be stored when coiled in a compact holder; the cylindrical coil shape is one shape of the bistable tape. When the tape-measure is used, the tape can take on a second shape where the axis of its curvature changes, and it gains the useful ability to maintain its rigidity (to a certain extent) as a ruler-like object to reach otherwise inaccessible points of measurement. Bistable laminates can be used in much the same way in aerospace applications while having the added benefits of being stronger and lighter, as will be discussed in the next section introducing the use of composites in aerospace.

2.1 Aerospace Composites

Fiber-reinforced materials are a natural choice for aerospace structures because of their stiffness and strength gains that can be achieved without sacrificing weight. Historically, the adoption of such materials in the aerospace industry most likely began in the 1950s with applications for missiles [3]. Since then, the industry has seen the adoption of increasingly advanced composite materials with many types of laminate and honeycomb structures, lending themselves to airliners such as the Boeing (Chicago, IL) 777, 787, and Airbus (Blagnac, France) A380, as well as many other aircrafts that keep the international world connected. This is not to mention military aircraft and drones, which rely heavily on composite materials. It is no exaggeration that whichever company (or nation) can get ahead in the game of fiber, polymer, and metal lamination will be a huge advantage, which is exactly why research into new composites is so well funded.

Table 2.1 Important events in the history of aerospace composite usage. [3]

First fiberglass boat	1942
Invention of filament winding	1946
Filament winding in missile applications	1950s
High strength carbon fiber in aircraft	1968
Kevlar fibers are developed	1973
Widespread composites applications in aerospace, marine, automotive, sports…	Late 1970's

2.2 Applications for Bistable Composites

Bistable composite laminates come into the picture around 1980 as stated before, but not until relatively recently have they been considered for applications, the two most notable of which are morphing structures and energy harvesting. Morphing structures in the aerospace context are components that can change shape significantly more smoothly and aerodynamically than conventional control surfaces, flaps, wings, or other structures. Aerospace is dominated by the need for greater aerodynamic efficiency. This is the natural evolution of the drive for greater efficiency by creating structures that can adapt to changes in the airflow around them or provide more efficient control for the pilot. The true realization of a highly adaptable morphing structure will probably be made up of multiple complementary technologies that all add up to allow high aerodynamic efficiency; however, bistable laminates are high on the list of technologies in terms of usefulness. Energy harvesting is the capture of mechanical energy for conversion into electrical power. The clever use of bistable laminates in this role could make them a good choice for collecting much-needed clean wind energy. Many studies have fabricated proof-of-concept designs for different applications.

Bowen et al. [4] explored the potential use for morphing structures for bistable composite laminates. This study involved attaching small plate-shaped piezoelectric actuators to the surface of a composite laminate to snap the laminate through to its alternate stable state. However, because only one actuator was attached to the laminates in this study, the laminate could not be snapped back into its original shape, as no voltage was required to maintain the laminate in the second shape. However, by placing a weight on top of the laminate, researchers found that they could create a system where the weight would push the laminate into the first stable state; when the actuator was supplied with voltage, the laminate snapped through to its other state, lifting the weight.

Mattoni et al. [5] propose a few different ways that bistable laminate structures could be used for applications in aircraft. These include variable-sweep morphing wings and morphing airfoils. The team created both numerical and experimental models of a wing spar with a web of steel tubes reinforced on both sides with CFRP with bistable portions. The structure was tested to determine the likely failure areas and load that it could withstand until buckling. The team also created a model of a trailing edge that by snapping the bistable portions of the structure through, the symmetrical trailing edge would deploy to act as a flap.

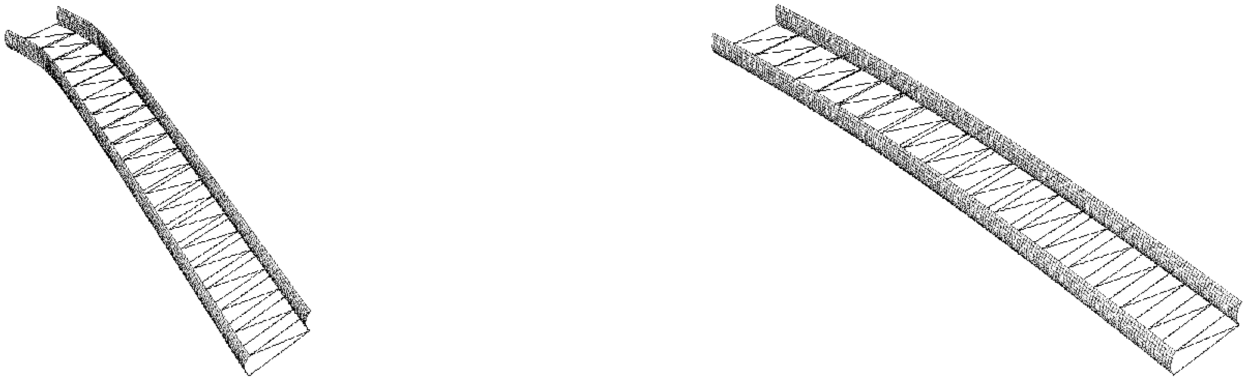

Figure 2.1 Design for wing spars with a bistable morphing section for variable sweep. [4]

Scarselli et al. [6] investigate an energy harvester concept using bistable laminates and state that it is advantageous to use bistable laminates in this application because unlike other designs, bistable laminates have a wide bandwidth of input frequencies. They conceptualized and fabricated an energy harvester that cleverly used a lever effect to cause large deformations when the bistable laminate in the harvester was loaded by a tensile testing machine that simulated environmental vibrations. The results showed that this design can harvest a large amount of power from this vibration.

2.3 Bistability Fundamentals

Bistability behavior is affected by a large number of variables, such as plate geometry, cure temperature and profile, ply layup, and ply thickness. Several papers were reviewed to learn about the fundamentals of bistable laminates, to find common points of confusion about this type of laminate, and to determine promising directions of study.

Zhang et al. [7] study the details of the “bistable” properties of anti-symmetric layups. This means that these types of layups have two different curvatures in which they can remain. Notably, the [30/-30/0/30/-30] layup (where the plies are stacked in sequence of the designation, with the numbers representing the laminate angle, 0 is horizontal, subscript numbers are repeated plies) exhibits this property. The team stated that the shapes of these layups are stable parallel and perpendicular to the edges of the sample.

Dano et al. [8] explain the relationships between the curvatures for a typical bistable unsymmetric laminate, in this case 3 families of laminates: $[-\theta_4/\theta_4]$, $[(90-\theta)_4/\theta_4]$, and $[(\theta-90)_4/\theta_4]$. θ is the laminate angle for the family, and can be varied. The paper theoretically explains that there are three possible states; however, the saddle shape is unstable and thus is never seen at room temperature in reality. For the $[-\theta_4/\theta_4]$ family, as the sample was cooled from the curing temperature, the laminate twist curvature κ_{xy} started to increase to a positive value. κ is the standard constant for measuring the curvatures and twist of a laminate. The curvatures κ_x and κ_y have two paths that can be taken, but will be roughly equal in magnitude and match sign.

In a later paper, Zhang et al. [9] study the snap action of a [35/-35/35/-35] layup by creating a specialized method to determine snapping loads. Notably, the layups were all semi-cylindrical shells created using a cylindrical mold in an autoclave. The team used a wedge-shaped object to push the center of the cylindrical shell downwards until the laminate snapped into another stable shape to measure the snap-through load. These results were also compared with the results from the non-linear finite element analysis using ABAQUS (Dassault Systèmes, Vélizy-Villacoublay, France). The team also showed that it takes more force to snap the laminate as the laminate becomes more curved.

The findings of Phatak et al. [10] suggest that the limitations of aspect ratio (AR) may not be as absolute as reported by Tawfik et al. [11] in their paper. Phatak et al. assumed that there is no critical aspect ratio and only the critical length determines the presence of bistability behavior. In other words, if both the length and width of a laminate are above the length where a square laminate of the same thickness becomes bistable, the rectangular laminate will also be bistable, regardless of the AR. The team proved this by determining the critical length for 2, 4, and 6 ply laminates and creating very high aspect ratio samples where the shorter side is held just above the critical length, up to AR 25. Combined with the fact that higher ply count laminates have longer critical lengths, this finding indicates that if an application calls for an AR that is too high for bistability, the only solution is to decrease the thickness of the laminate, which may not always be possible.

Finally, to connect the findings of these two studies to the measurement of residual stresses within the laminate during curing, it stands to reason that, based on the findings of Phatak et al., there is an average residual stress per unit area threshold value that must be met for the laminate to be bistable because if only a critical length is required on the short side, it is necessary for a per area stress to overcome other effects and create bistable behavior. This would explain the high-aspect-ratio samples of Phatak et al., because any increase in the total laminate area would result in a proportional amount of residual stress. This can be measured during curing using Digital Image Correlation (DIC).

The study by Giddings et al. [12] describes the work done with an Finite Element (FE) model using ANSYS (Ansys Software, Canonsburg, PA), which was created to study the shape of cured asymmetrical laminates and includes the effects of common manufacturing defects. According to the study, there are regions near the corners and edges of the typical multistable laminate where the curvatures are reversed, and this phenomenon is not considered by most models. The team was able to obtain very good correlations with a real-world laminate that they created after improving their FE model to consider more precise details regarding the resin-rich layers and ply thickness. Finally, the study demonstrated the effect of the thermal load on the laminate, which flattens as the temperature increases.

2.4 Computational and Analytical Work

In their later study, Mattoni et al. [13] explored a new analytical model that was created to be more robust than previous models by being able to model more than the typical free-free conditions to which other models were limited. The team stated that to account for other boundary conditions, the existing models must be altered to not assume a constant curvature. In fact, the model has a parabolic function for the curvatures, contrasting the constant-across-domain assumptions of the other models. The team then showed that the model can be applied to a compound plate, which has regions of symmetric and asymmetric layups.

Betts et al. [14] state that imperfections in real-life laminates play a significant role in the shape at room temperature. After creating a few different bistable layups, their team used a system of three cameras and motion analysis techniques to measure the out-of-plane displacement at room temperature. The team found that there were differences in the experimental results as compared to the analytical model due to the presence of thin resin layers and free edge effects, which increased the stress at the edge of the laminate, and therefore also the curvature.

2.5 Recent Research

Zhang et al. [15] propose many ways to connect single bistable sections into larger multistable plates of varying size. These resulting plates have several states, which are the sum of the number of states of all bistable sections. The combined plates consist of deformation elements and transition elements. The deformation elements are the primary shape-changing unsymmetric elements, while the transition elements provide a smooth transition between these bistable sections and are made from small opposite antisymmetric sections.

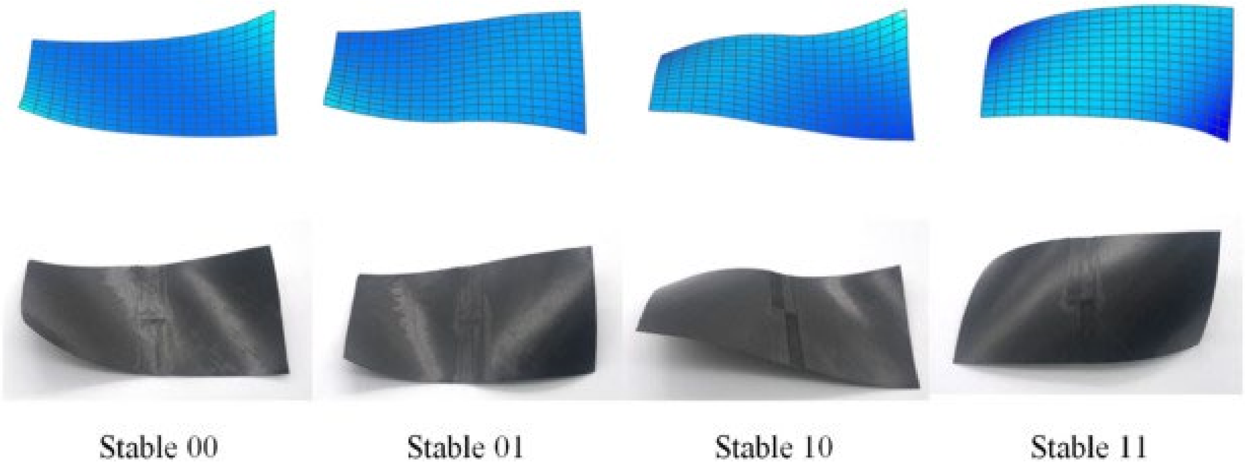

Figure 2.2 Different configurations of tessellated bistable laminates that show the multitude of potential shapes when combining different layups. [15]

Anil kumar et al. [16] do further research into actuation of bistable laminate structures using macro fiber composite (MFC) actuators, which is a common alternative to shape memory alloy (SMA) actuators as seen in other research. Some advantages of MFCs are their low profile and high performance, and the group theorizes that distributing smaller MFC actuators over the entire surface of the bistable laminate could be more efficient than the conventional approach of placing one large actuator in the center of the laminate. This has an adverse effect on the bistability of the laminate because it tends to flatten it. The team used semi-analytical and FEA methods as well as experiments to study the effect of actuator placement and introduced variable-stiffness laminates instead of conventional cross-plies.

Liu et al. [17] research dynamic characteristics of bistable laminates in order to identify possible methods of actuation using resonance to their advantage. The team formulated an analytical model based on the theory of minimization of potential energy, as well as an ABAQUS FEA model. The natural frequencies of the laminates based on their width were determined, and these data were used in frequency sweep experiments where the bistable laminate was excited using a shaker device and snap-through and snap-back behavior was observed when the frequency of vibrations caused the amplitude of deflections to rise sharply owing to resonance. It was concluded that using these frequencies could aid in the actuation schemes.

3 Experimental Methodology

To achieve the research objectives, unsymmetrical [0/0/90/90] CFRP samples were produced and analyzed in various ways, both during the curing process and after successive rounds of machining. From this, the base level of bistability for the lab samples was determined, as well as the effect of post-cure machining of the type that is commonly used in industrial applications CFRP structural components. By carefully tracking the bistability behavior throughout the entire process with several different parameters such as curvature, residual strain, and snap-through load, one can compare with the analytical and finite element models to obtain an informed characterization of this type of laminate.

3.1 Materials

Unidirectional carbon fiber prepreg CFSJ-1500H (Composites One LLC, Lakeland, Florida) with manufacturer provided material properties are given in Table 3.1, was the primary material used in this study. Apart from that, the breather and peel ply used in the layup were procured from Fiberglast (Fibre Glast, Brookville, OH).

Table 3.1 List of material properties for the CFRP prepreg in this study.

Material Property	**Value**	**Unit**
Elastic Modulus E_1	130×10^9	Pa
Elastic Modulus E_2	12×10^9	Pa
Shear Modulus G_{12}	4.8×10^9	Pa
Poisson's Ratio v_{12}	0.35	

Mold release FibRelease 1153 from Fibre Glast is also necessary to remove the samples from the aluminum tool plates. A reasonable supply of these plates should be kept on hand, and the plates should be at least large enough to fit the largest sample area plus room for vacuum probes. To apply the speckle pattern, Rust-Oleum white spray paint primer (RPM International Inc, Medina, OH) was utilized. Finally, GS sealant tape (General Sealants, Industry, CA) was used to adhere the vacuum bagging to the tool plate.

3.2 Autoclave Processing DIC Analysis

The main procedure that forms the basis for the experimental work in this study is the processing of unidirectional CRFP samples within an ASC (ASC Process Systems, Valencia, CA) Econoclave 2x4 autoclave specialized for research at Embry Riddle Aeronautical University. This autoclave has pressurization (not used in this study) and an integrated vacuum pump that is run at -350 torr on all experiments. It has a 61cm by 122cm working interior and is lit internally using a bright 150W halogen bulb. This model features viewports allowing twin Digital Image Correlation (DIC) Correlated Solutions 6MP cameras (Correlated Solutions Inc, Columbia, South Carolina) to observe the sample during curing. Preparation for a cure cycle with the setup begins by cutting several plies of CFRP of the desired size off the large rolls that are kept in a walk-in freezer that keeps the prepreg at around -10˚C when not in use.

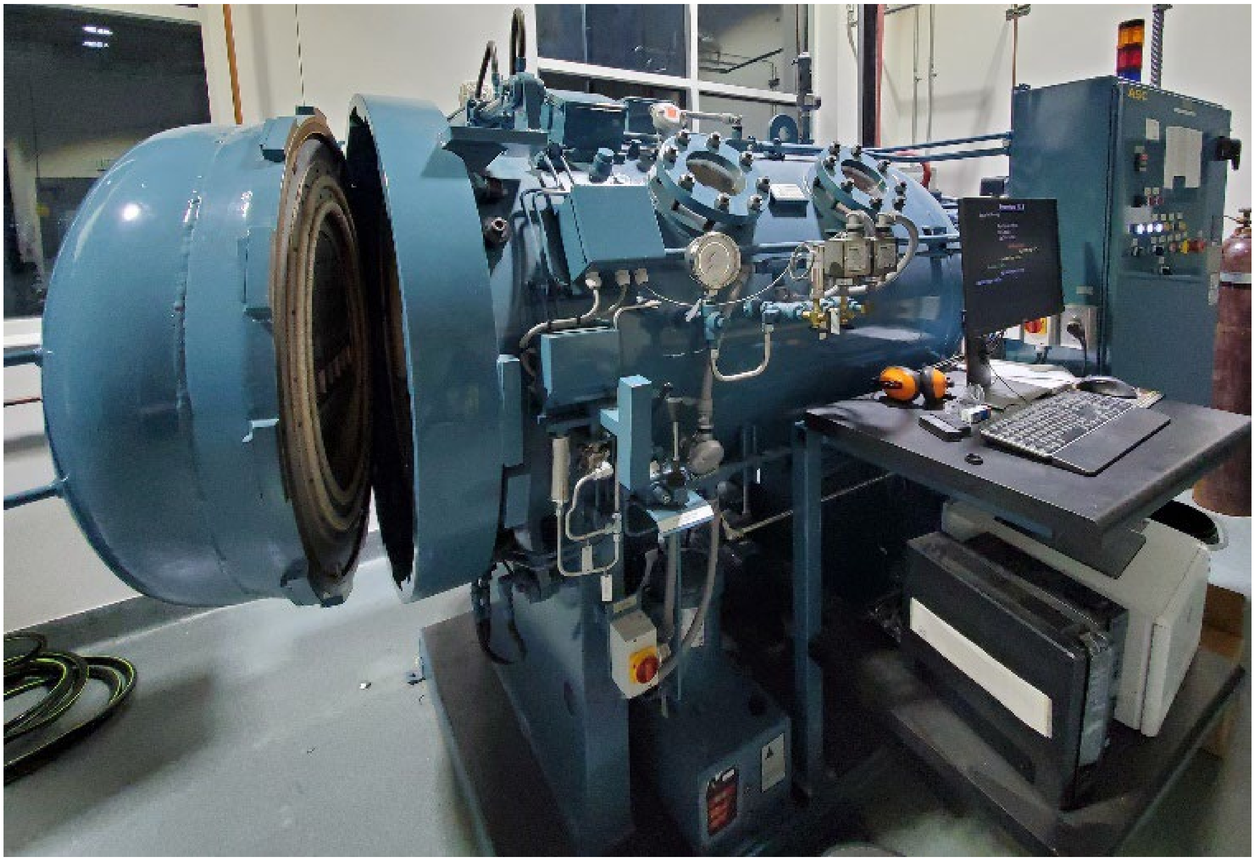

Figure 3.1 View of ASC Econoclave 2x4 with viewports and controlling Dell (Round Rock, TX) PC.

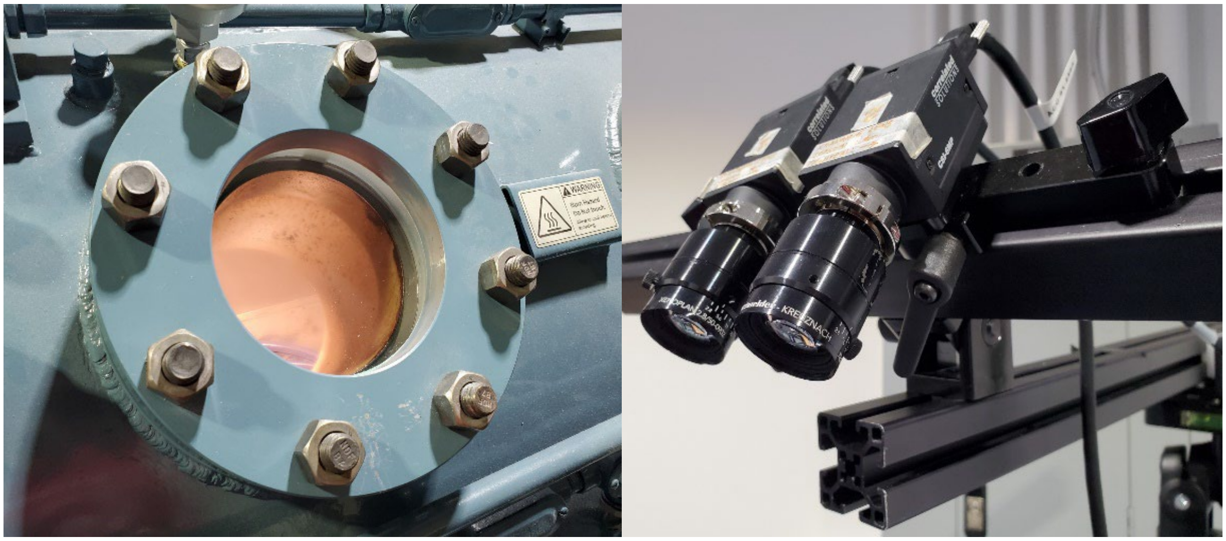

Figure 3.2 Close up of viewport and Correlated Solutions DIC cameras.

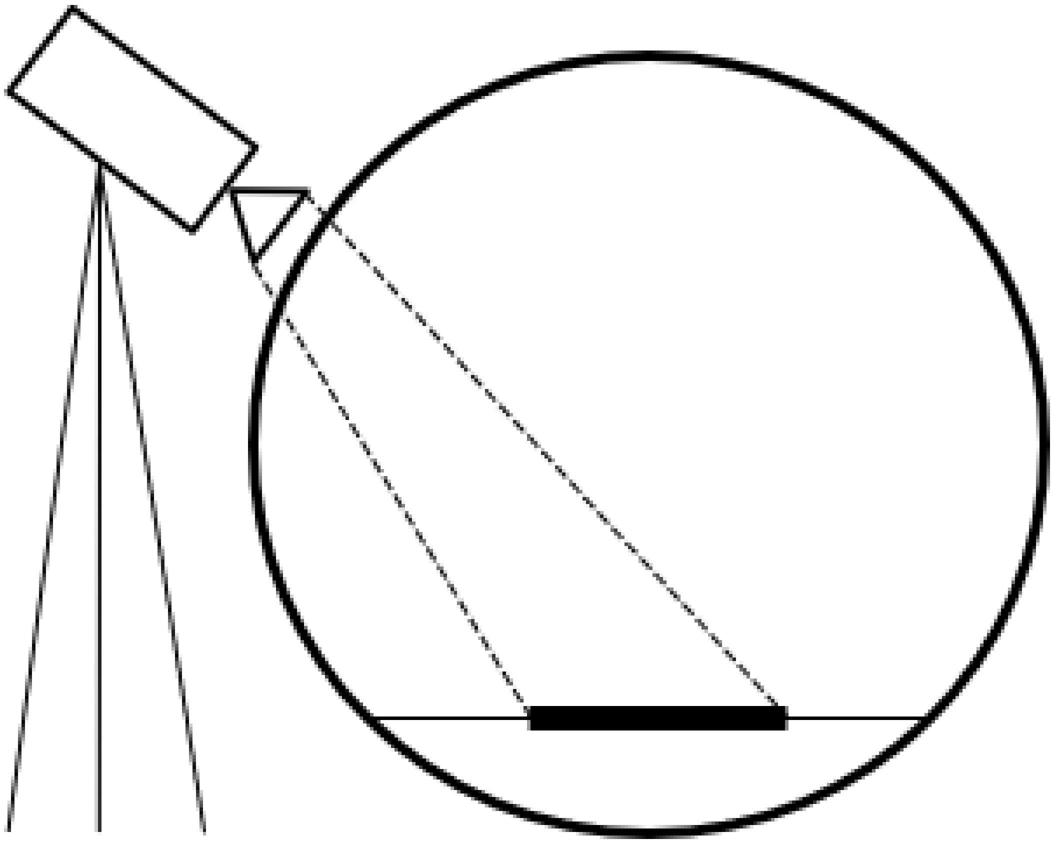

Figure 3.3 Schematic diagram of camera Field of View (FOV) on CFRP sample within autoclave. The camera angle and sample position were adjusted until the minimum amount of glare was achieved.

To set up the experiment, it's recommended to have all equipment at-hand so that the setup can be completed while the prepreg from the freezer is still cool. The equipment and some of the materials required for this process is shown in Figure 3.4. Included is a paint roller for pressing plies and sealant tape flat, as well as the required vacuum probes and the 7mm size calibration tile (Corellated Solutions). The portable electric cutting tool eases the cutting of the materials significantly. Also helpful are Scissors and a permanent marker.

Figure 3.4 Selected equipment and materials. Note the calibration tile in the upper center of the image. The specific spacing and pattern of the dots on this tile allow the cameras to have a base for their analysis.

Begin by placing a perimeter of sealant tape around the edges of the tool plate and then apply a small amount of mold release. The layup of the prepreg plies can now begin. The plies are stacked until the last layer, where a speckle pattern for the DIC cameras is painted on. There are many alternate ways to do this, and it is up to the reader to choose a painting method that will work best for their setup. In this case, carefully spraying droplets of spray paint was used. This can be done carefully by hand by gently pressing the spray can cap so only minimal paint is dispensed, then angling the can so that proper sized droplets of around 1-2mm in diameter drop onto the entire surface of the laminate. Good coverage of speckles is required. Ensure that the entire surface of the sample is covered with well-spaced and sized spots of paint. Stack this ply onto the rest and cover everything using vacuum bagging.

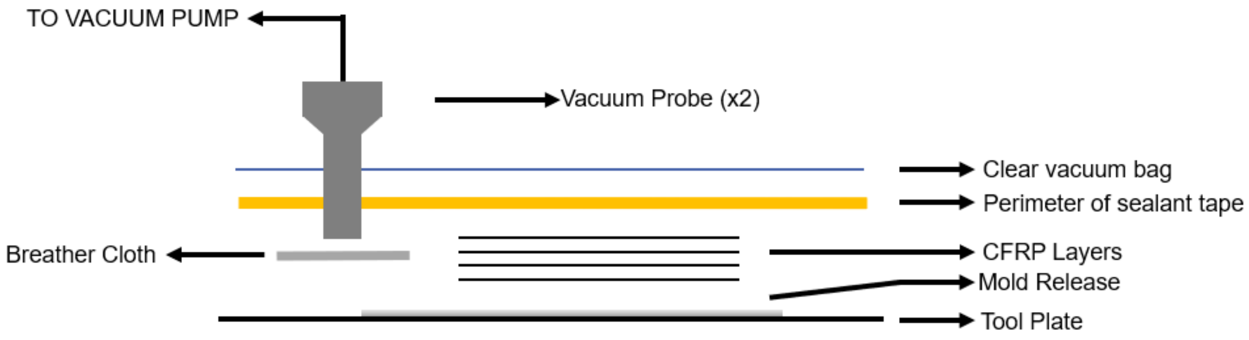

Figure 3.5 Exploded view of a sample ready to be placed in an autoclave.

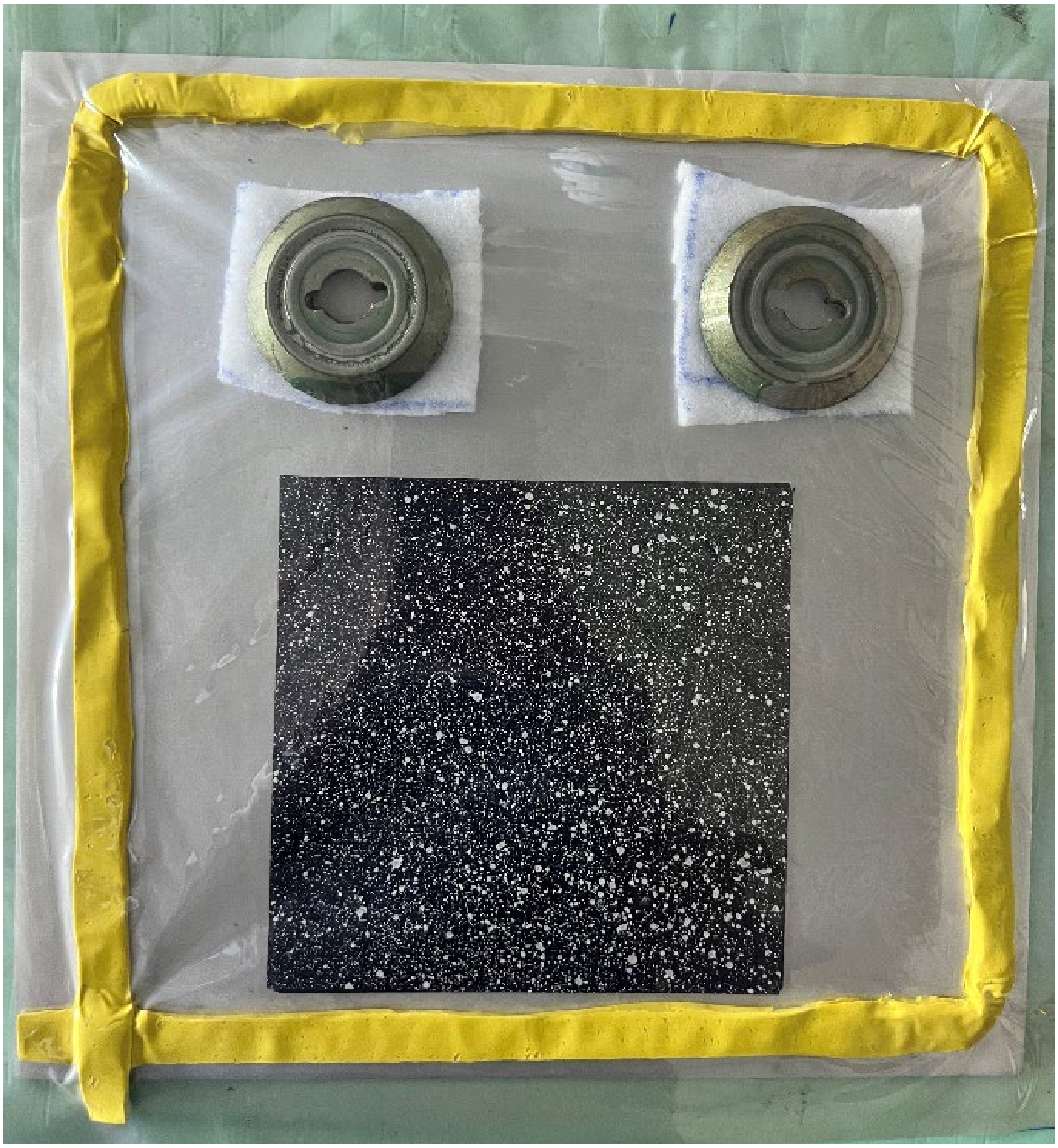

Figure 3.6 Top view of a 152.4 cm square autoclave sample with a speckle pattern for DIC.

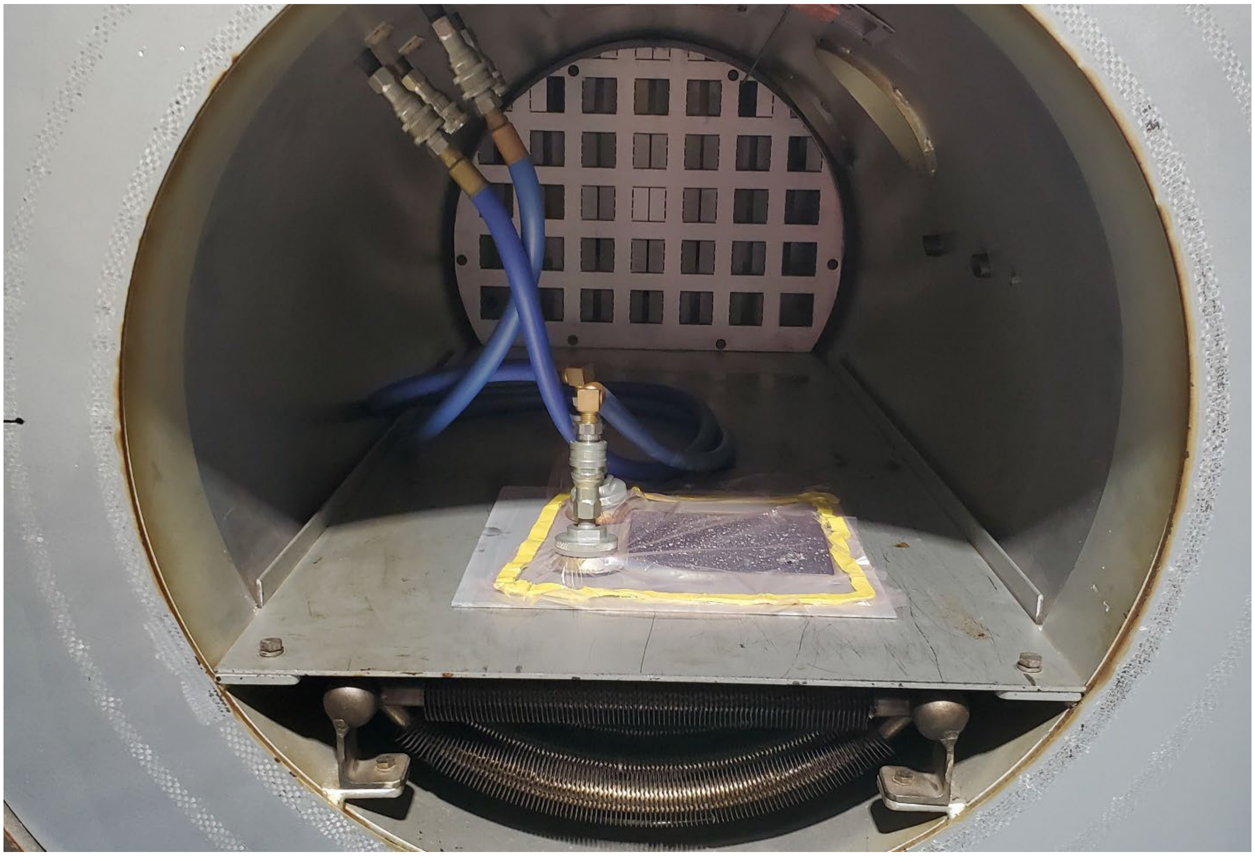

Figure 3.7 Sample setup within autoclave, viewport opening can be seen in upper right. Make sure to use two vacuum probes, one for vacuum source, and the other for vacuum probe.

Before or during the sample preparation process, the monochromatic DIC cameras from Correlated Solutions can be focused and calibrated using a special calibration tile. Use this tile, shifting and angling it, to take ~100 images to be used by the cameras for calibration. During curing, both cameras take an image every 30 s using VIC-Snap, an automatic image-taking software for the cameras. Using this software is simple: simply create a folder for calibration and speckle images and press the spacebar to manually take calibration images. Use the timed capture function for the images of the sample. These images were used by the VIC-3D software to track the random speckles on the sample to determine positions, displacements, and strains. In VIC-3D, calibrate the software by inputting the calibration tile images, then analyze the speckle images using the area-of-interest and strain calculation tools. This data is tabulated into Excel (Microsoft Corp, Redmond, WA).

The cure cycle is formatted in the autoclave control software as a list of steps in which parameters such as dwell and cure temperatures, cure period, heating, and cooling rates can be modified. For most tests, a cure profile that was found to reduce bubbling/wrinkling on the surface of the samples [18] was used. This profile dwelled at 80°C for 30 min before curing at 130°C. For selected samples, this cure profile was modified to measure its effect on the room-temperature curvature of the samples. In this modified or "interrupted" cure profile [19], the sample is rapidly cooled to room temperature upon first reaching the cure temperature, then heated again, and the cure continues as normal. This profile is shown in Figure 3.9.

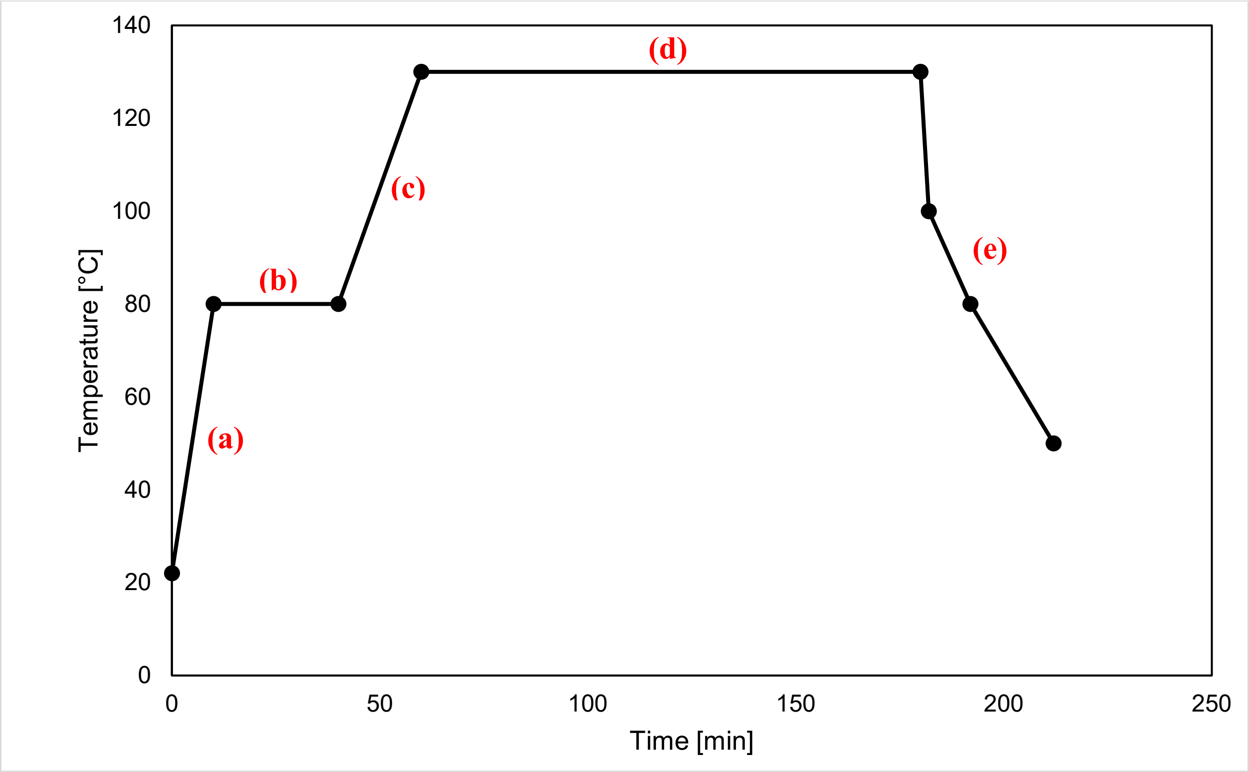

Figure 3.8 Normal "dwell and cure" cure cycle. The recipe for the autoclave consisted of five steps. a: Initial heating from room temperature at 5°C/min. b: 30 min "dwell" period at 80°C to reduce wrinkling and improve DIC accuracy. c: 2°C/min heating to curing temperature of 130 °C. d: 120-min cure period. e: Unlimited cooling rate phase to bring the sample to 50°C for removal from the autoclave.

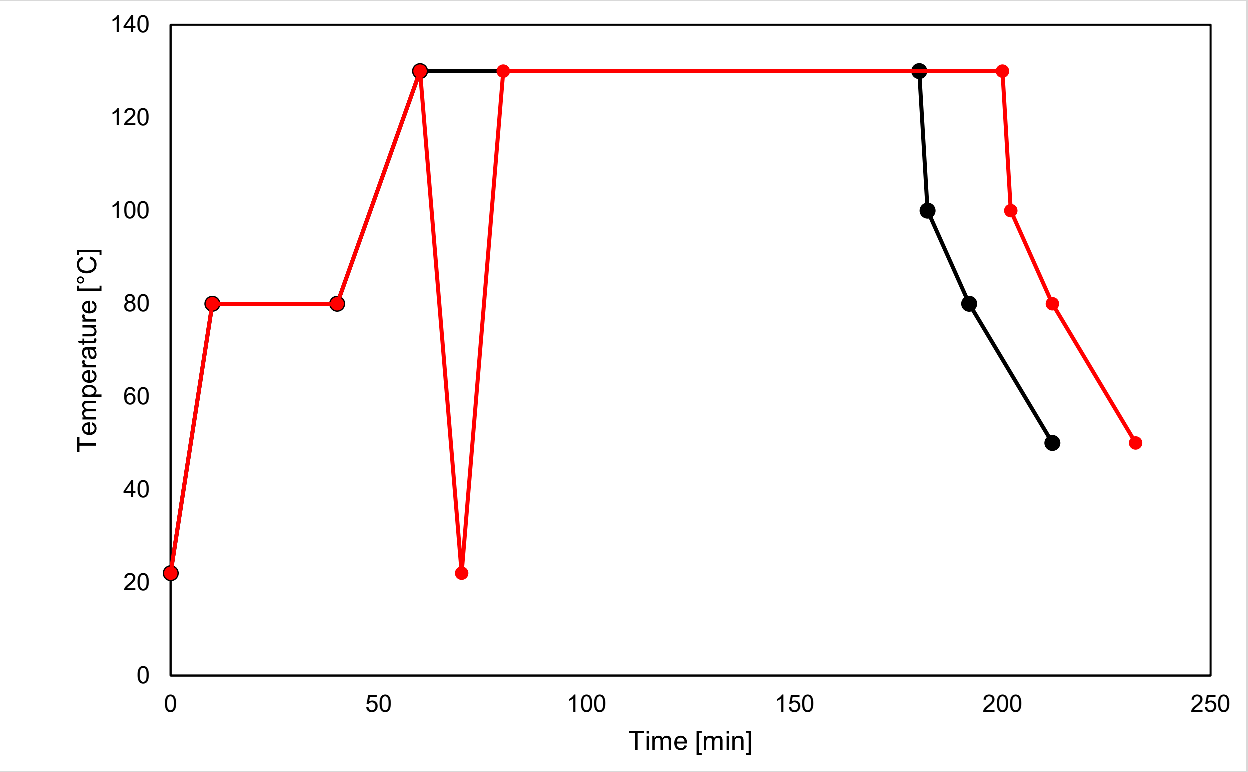

Figure 3.9 Interrupted cure cycle (red) compared with the normal cure cycle.

Steps to improve the accuracy of DIC cameras are paramount for the acquisition of reliable strain results. Minimizing glare from the light source, ensuring that the sample does not shift within the autoclave, applying a good speckle pattern, and reducing bubbling or wrinkling on the sample surface are the most important ways to ensure camera accuracy. Glare can be removed from the image view by shifting the initial sample placement and the camera angle. It is usually not possible to remove all glare from the sample surface because the vacuum bagging is very reflective, but increasing the area that is within acceptable lighting levels for the cameras also increases the number of speckles the DIC software can analyze and provide a more accurate representation of the strain over the entire surface. If the tool plate holding the sample shifts during the cure cycle (this is usually due to the vacuum probes twisting the tool plate that the sample is on), the DIC software will register this as erroneous extra strain and produce unacceptable results. To mitigate this, the initial position of the tool plate is marked with a marker, and pieces of vacuum sealant are placed to adhere its corners to the autoclave base. As previously stated, there are many different methods for applying a speckle pattern to the sample surface for DIC analysis. Whichever method is chosen, it is important to ensure that an acceptable spread of reasonably sized speckles is applied (about 1-2mm). Speckles that are too small will not be picked up by the DIC cameras; however, speckles that are too large are far less accurate. It is also important to not leave any large spaces on the sample without suitable speckles, as these areas will not be able to be analyzed by the DIC software. In this study, great care is taken to regulate the spray of the spray paint can so that only paint droplets of the correct size hit the laminate. This can be done by angling the can so that particles that are too light and small spray too far to hit the sample, and only the heavier droplets fall on the sample. This method is very accurate if done correctly, but it's recommended to practice spraying on a piece of black paper before trying on actual samples to get a feel for this unconventional way of using a spray can.

Over the course of the curing cycle, resin bubbles or wrinkles formed on the surface of the sample. These features usually reflect additional light and cause localized glare at these spots, thereby reducing the DIC accuracy. Reducing resin wrinkles and bubbles on the sample surface is the most difficult of these three methods for improving accuracy, but there are some steps that were found to greatly reduce them. The first, as mentioned previously, is to adopt a cure cycle that has been shown to reduce bubbling, as in this study. Second, it is also very helpful to lay up the plies of the sample as neatly as possible, ensuring that air bubbles are not present between plies, and the surface of each ply is flat using a paint roller or similar tool. Wrinkles can also form on the surface of a sample when a vacuum pressure is first applied to the sample. It is recommended to pull the bagging taut over the surface of the sample before turning on the vacuum. Figure 3.10 illustrates the effect of bubbling on DIC accuracy, as well as the effects of having a poor speckle pattern on the sample.

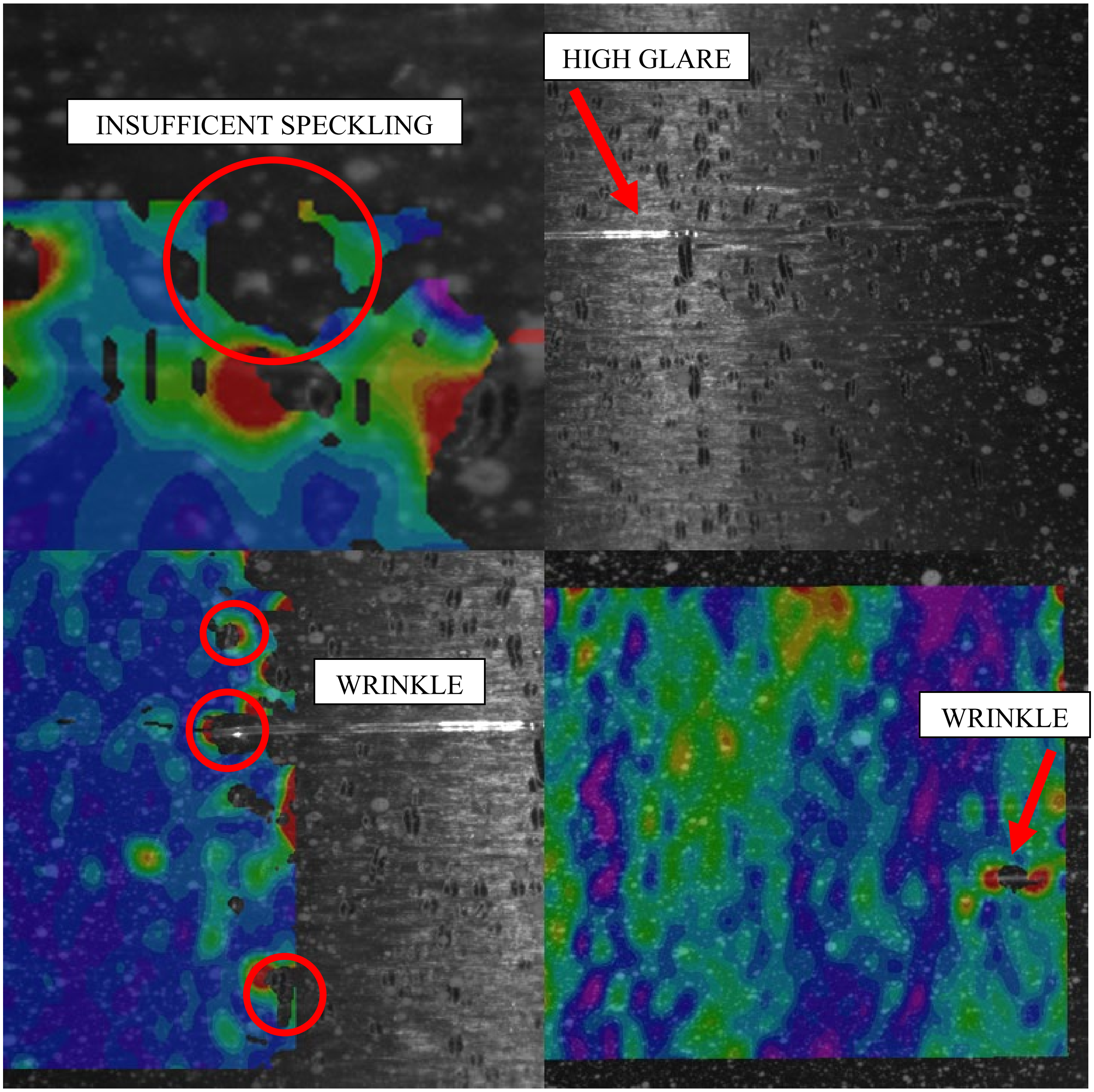

Figure 3.10 View of common flaws that affect DIC accuracy in laminate normal strain in the direction of the x-axis (e_{xx}) strain contour plots. Top left: A zone of poor-quality speckles, uncolored because the DIC software was unable to analyze them in the contour plot of the sample. Top right: Band of glare, wrinkle in vacuum bagging, and resin bubbles. Note the increased glare of the wrinkles. Bottom left: Effect of wrinkles and bubbles on DIC analysis, causing holes in the contour plot. Bottom right: DIC contour plot of fair quality with a good speckle pattern and no bubbles, only interrupted by a wrinkle.

After the curing cycle was completed, the samples were carefully removed from the tool plate, and their side lengths (L_1, L_2) and center heights (h_1, h_2) off a flat surface were measured. Using the equation below, the curvature of the laminate can be determined: [20]

$$h^2 - 2hR + R^2 sin^2\left(\frac{L}{2R}\right) = 0 \tag{3.1}$$

Where R is the radius of the laminate curvature and is the inverse of the curvature. These data can then be compared with the analytical and finite element models.

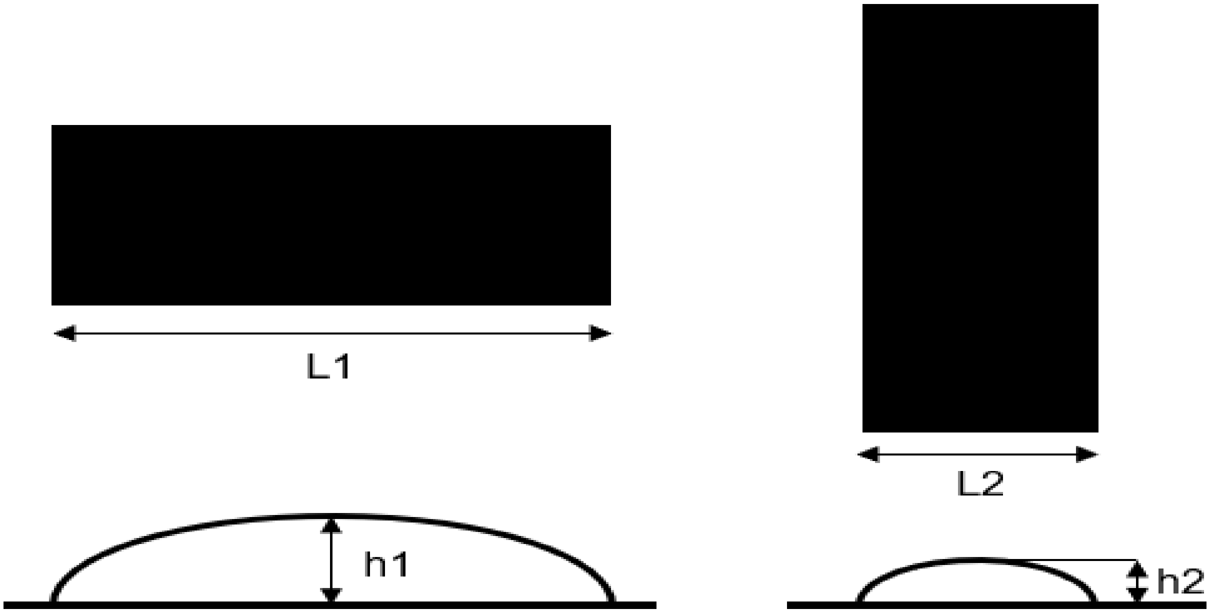

Figure 3.11 Diagram showing the four measurements needed to find the laminate curvatures in both stable shapes.

Table 3.2 List of samples produced for research. Samples labeled “Water Jet Cutter” were machined down from originally being 15.24cm x 15.24cm samples, to 15.24cm x 10.16cm, and then to 15.24cm x 7.62cm.

Sample ID	**Layup**	**Length [cm]**	**Width [cm]**	**Cure Processing**	**Post Processing**
661 (9-14)	$[0_2/90_2]$	15.24	15.24	Dwell + Cure	Water Jet Cutter
662 (9-27-1)	$[0_2/90_2]$	15.24	15.24	Dwell + Cure	Water Jet Cutter
663 (9-27-2)	$[0_2/90_2]$	15.24	15.24	Dwell + Cure	Water Jet Cutter
641 (9-17)	$[0_2/90_2]$	15.24	10.16	Dwell + Cure	None
642 (9-19)	$[0_2/90_2]$	15.24	10.16	Dwell + Cure	None
643 (9-20)	$[0_2/90_2]$	15.24	10.16	Dwell + Cure	None
631 (9-22)	$[0_2/90_2]$	15.24	7.62	Dwell + Cure	None
632 (9-24)	$[0_2/90_2]$	15.24	7.62	Dwell + Cure	None
633 (9-25)	$[0_2/90_2]$	15.24	7.62	Dwell + Cure	None
621 (9-25-1)	$[0_2/90_2]$	15.24	5.08	Dwell + Cure	None
622 (9-25-2)	$[0_2/90_2]$	15.24	5.08	Dwell + Cure	None
623 (9-26)	$[0_2/90_2]$	15.24	5.08	Dwell + Cure	None
INT1 (2-7)	$[0_2/90_2]$	15.24	15.24	Interrupted Cure	None
INT2 (2-11)	$[0_2/90_2]$	15.24	15.24	Interrupted Cure	None

Figure 3.12 Range of samples cured in autoclave.

3.3 Snap-Through Load Testing

A Chatillon CS225 Force Tester (Johnson Scale Co, Montville, NJ) seen in Figure 3.12 was used to test the snap-through load of the cured samples, with the maximum force set to 15 N. The samples were loaded at a constant speed of deflection at a rate of 0.05 mm/s. A list of equipment for these tests is as follows:

1. Upper compression test platen.
2. Flat, low friction surface plate of appropriate size to be placed on the tester.
3. Marking tools to mark the center of the laminate.
4. USB drive to record data.

To set up the machine for this type of test, the bottom platen or tension grip was removed and a smooth tool plate was placed on the bottom surface of the tester. Then, a small-diameter platen was placed on the load cell to press against the laminate, as shown in Figure 3.13. The load response is recorded as the machine moves the platen downwards until the popping noise is heard, which is indicative of the laminate snapping through. This is caused by the thermal stresses imparted on the laminate from the curing process. As the deflection changes, the two plies perpendicular to the direction of original curvature begin to overpower the other two plies, snapping the laminate into another shape with the residual stress present within the plies due to thermal shrinkage. The maximum load achieved during this process was considered as the snap-through load. Samples of the load response for 2 sizes of sample can be seen in Figure 3.15.

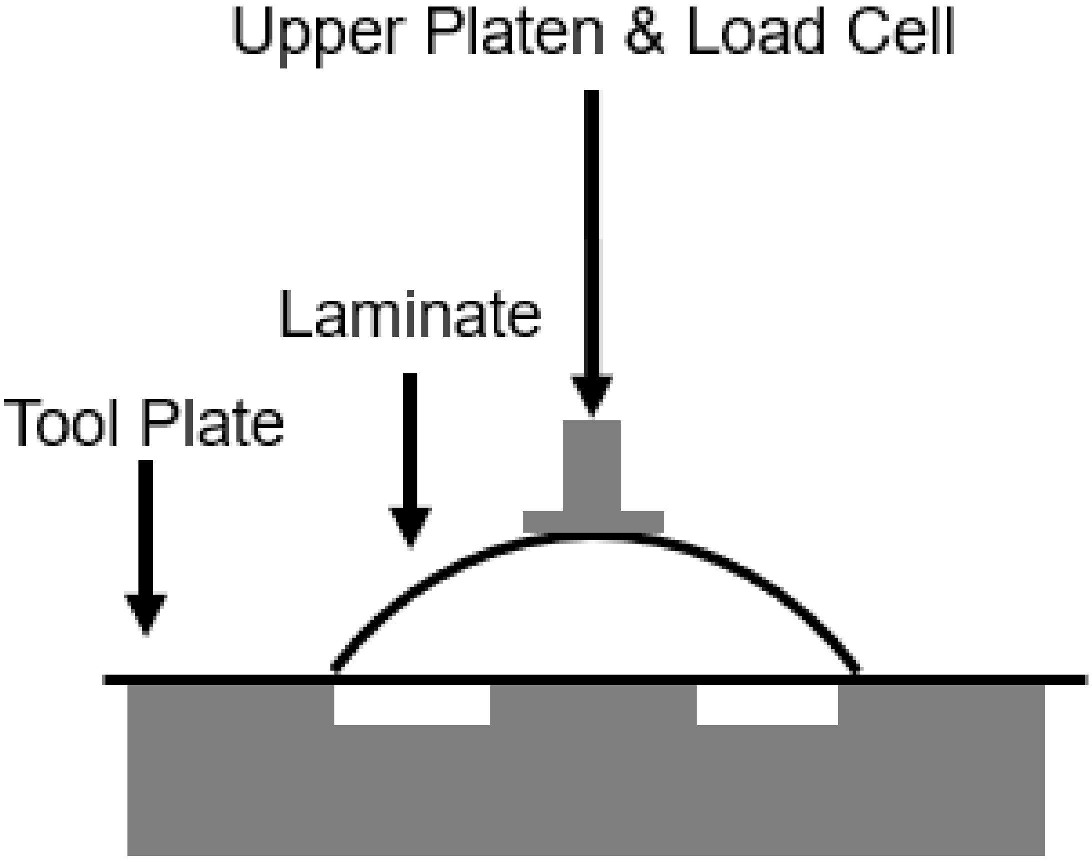

Figure 3.13 Experiment diagram of snap-through testing. All edges of the laminate are free.

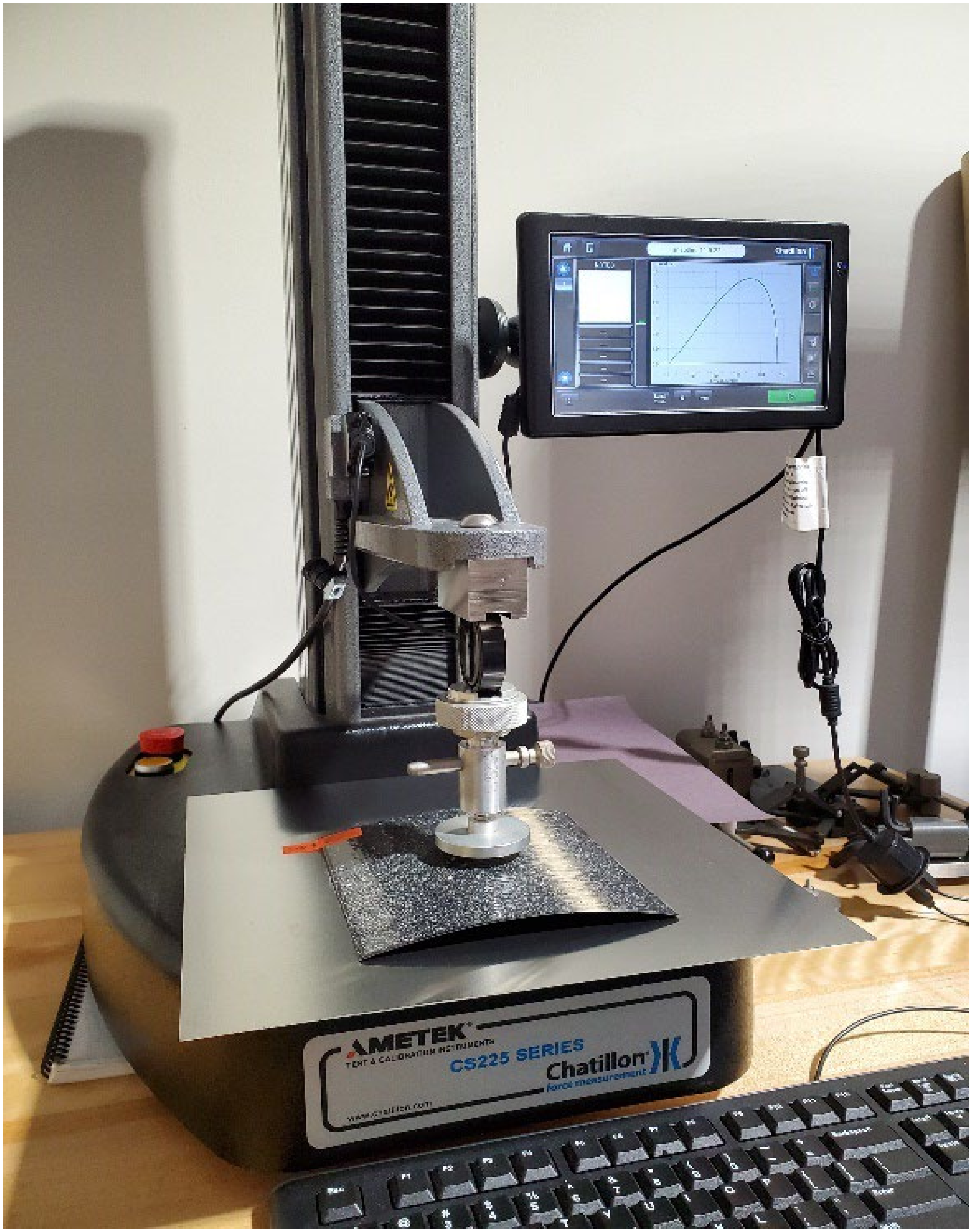

Figure 3.14 Image of the force tester setup with laminate before being snapped through.

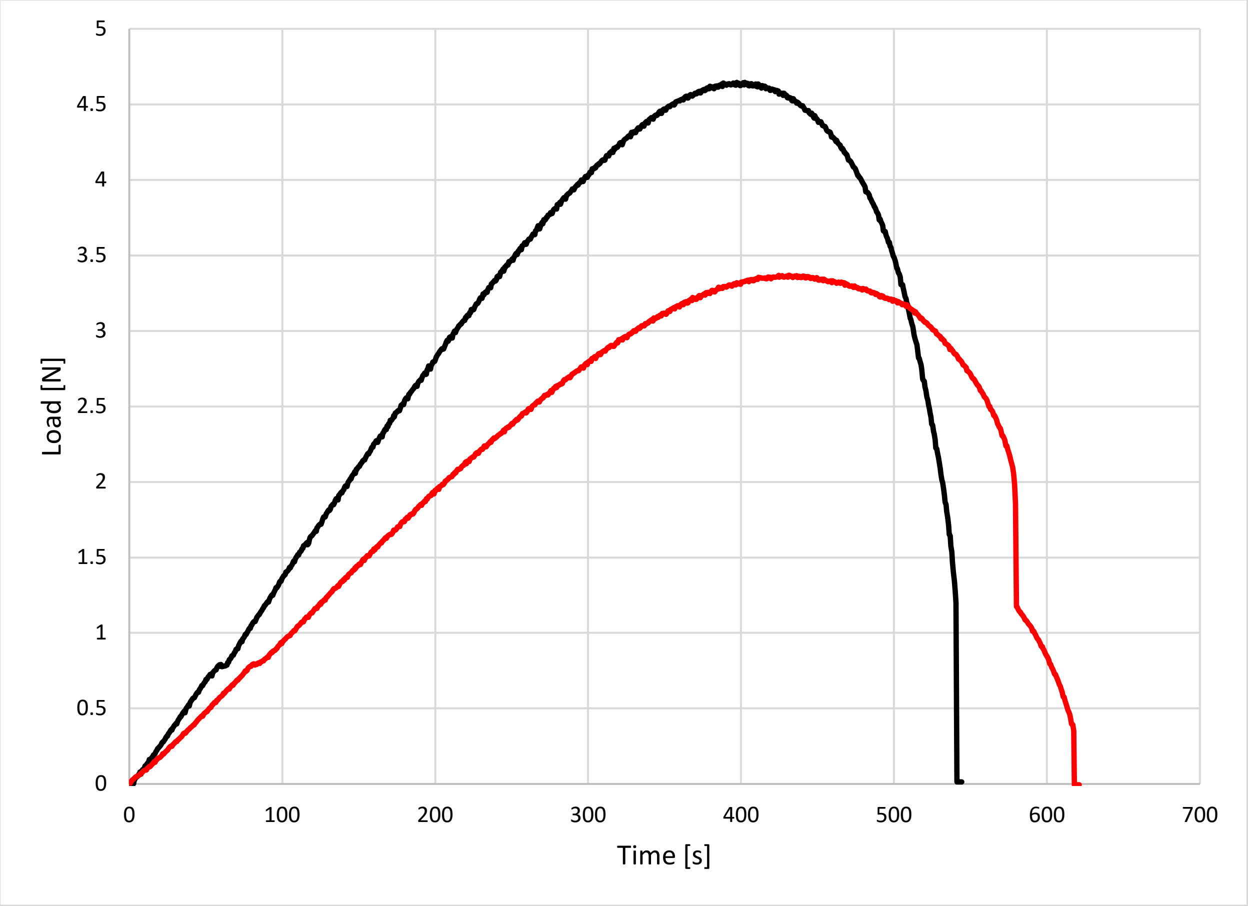

Figure 3.15 Plot of the load response for the snap-through load tests. It can be seen that the square 15.24cm x 15.24cm sample (black) carries more residual stress than the 15.24cm x 10.16cm sample (red), which means more force is required to change the shape of the larger sample.

3.4 Post Cure Machining

To observe the effects of post-cure machining on bistable laminates, 15.24 cm-by-15.24 cm [6 in x 6 in] samples (the largest produced in this study) were cut using an OMAX (OMAX Corp, Kent, WA) Maxiem 1515 water jet cutter to make clean, straight cuts without the chance of damaging the plies that are present with non-specialized metal-bladed table saws. A list of equipment for cutting samples in this manner is below.

1. Tool plate
2. Water-proof heavy duty tape
3. Marking tools
4. Clamps
5. 80-grit garnet for water jet abrasive hopper

After starting the pumps, computer, and the water jet itself, the samples were tightly taped to a tool plate so that they were flat for the cutting process. This is recommended over the typical CFRP cutting procedure of simply clamping the laminate to the water jet cutter because the curvature of this type of laminate can be significant, and the pressure from the water jet might cause the laminate to change shape mid-cut which would have adverse effects. The tool plate is clamped to the water jet cutter fins in the normal manner. In the OMAX MAKE software, it is recommended, after inputting the correct material and thickness, to modify the settings so that the machine pierces using low pressure. The "Very Brittle Material" setting was also used during this study with good results and a lack of delamination of the plies. It is recommended to set a larger thickness than the thickness of the laminate so that the water jet cleanly cuts through both the laminate and the tool plate so that bubbles and water are not trapped between them. Submerge the laminate under a thin layer of water during the cut. A straight cut using the saw function is made to shorten one side, and the side lengths and curvatures of the samples were re-measured. This process was repeated as the side length was reduced from 15.24 cm [6 in] to 10.16 cm (4 in), 7.62 cm (3 in), and finally 5.08 cm (2 in).

Figure 3.16 OMAX Maxiem 1515 water jet cutter of the kind used to cut samples. [21]

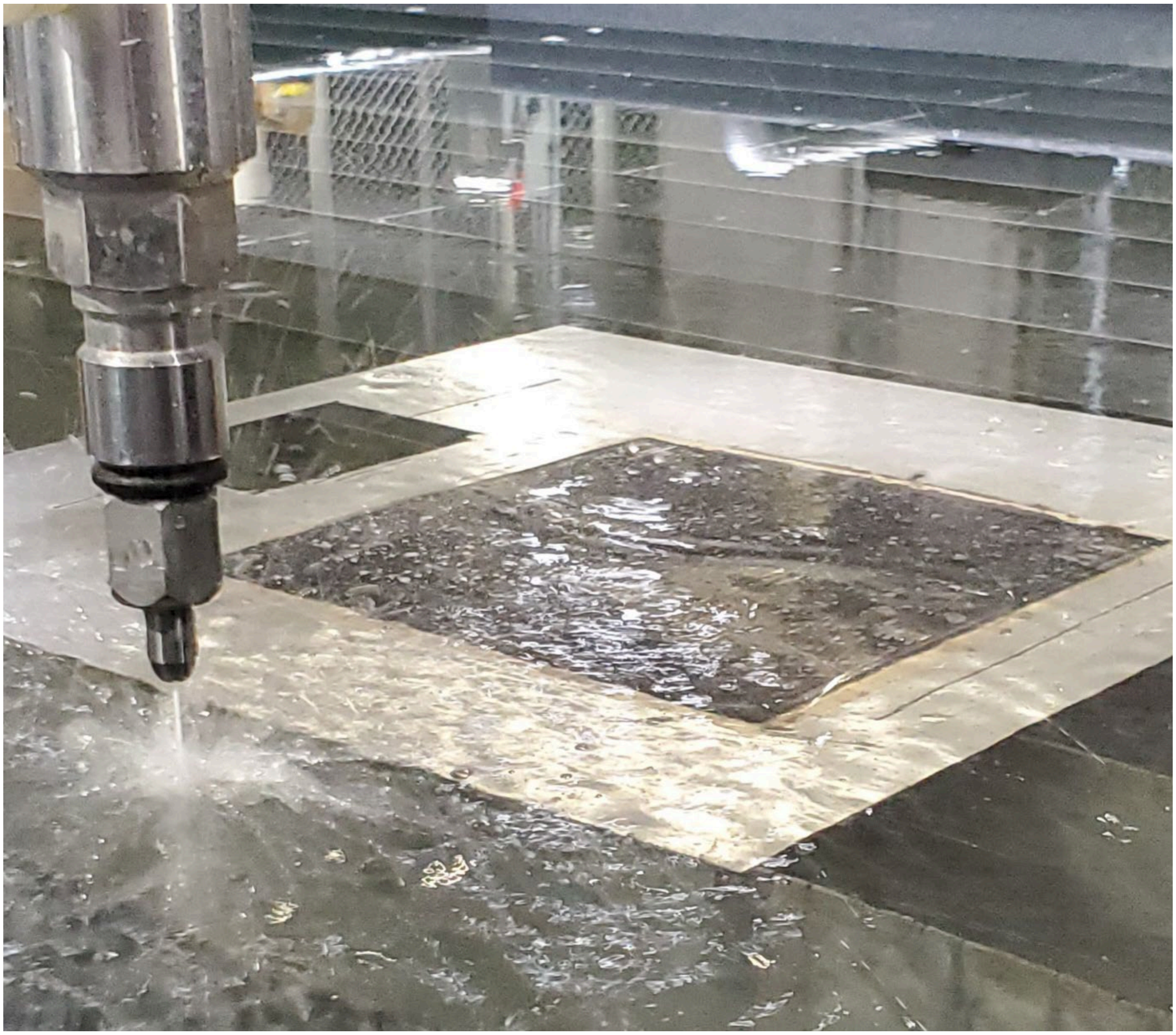

Figure 3.17 Water jet cutter in operation, next to laminate sample taped to tool plate. It is necessary to make sure the laminate is as flat as possible for this process.

4 Analytical and Computational Methods

To correlate with the experimental results, an analytical model and ANSYS FEA model were developed. The analytical model is based on the extended CLT theory and can be used for computationally inexpensive analysis to compare with experiments. The methods used in the FEA model additionally account for the properties of the resin by using an advanced cure simulator.

4.1 Analytical Model

The improved model Hyer created in his paper [2] is a robust and straightforward way to correlate results from experiments with a nonlinear extension of Classical Laminate Theory (CLT). The model uses von Karman approximations for the strain field, which are modified to better represent the variation in strain over laminates of this type, validated because the out-of-plane displacements are larger than the laminate thickness. The basis of the model is the assumption that the laminates can become one of three shapes at room temperature according to the following equation:

$$w(x,y) = \frac{1}{2}(ax^2 + by^2) \tag{4.1}$$

where a and b are constants, the solutions of which, shown in Figure 4.1, determine the shape of the laminate. w is the z-axis displacement of the laminate, with x and y being the in plane axes, and u and v being the displacement in those respective axes.

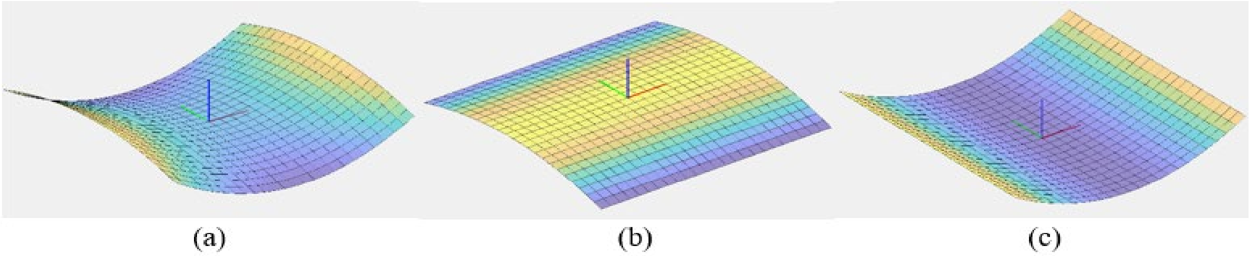

Figure 4.1 Types of room-temperature laminate shapes predicted by Hyer's model. (a): *a* is positive and *b* is negative. (b): $a > 0$ and $b = 0$. (c): $a = 0$ and $b < 0$.

Because the out-of-plane displacements are much larger than the laminate thickness, the in-plane strains ε_x, ε_y, and ε_{xy} for this model become:

$$\varepsilon_x^0 = \frac{\delta u^0}{\delta x} + \frac{1}{2}\left(\frac{\delta w}{\delta x}\right)^2 \tag{4.2}$$

$$\varepsilon_y^0 = \frac{\delta v^0}{\delta y} + \frac{1}{2}\left(\frac{\delta w}{\delta y}\right)^2 \tag{4.3}$$

$$\varepsilon_{xy}^0 = \frac{1}{2}\left(\frac{\delta u^0}{\delta x} + \frac{\delta v^0}{\delta y} + \frac{\delta w}{\delta x}\frac{\delta w}{\delta y}\right) \tag{4.4}$$

Then, these equations are fitted to the shapes of the model using a and b, and four other constants after reasonable approximations of the strain field and laminate geometry are used.

$$\varepsilon_x^0 = a_1 + a_2 x^2 - \frac{aby^2}{4} \tag{4.5}$$

$$\varepsilon_y^0 = b_1 + b_2 y^2 - \frac{abx^2}{4} \tag{4.6}$$

$$\varepsilon_{xy}^0 = 0 \tag{4.7}$$

These equations were used to minimize the potential energy of the laminate.

$$W = \int_V \omega dV \tag{4.8}$$

Where *V* is the volume and *ω* is the strain energy density. *ω* is a function of the six constants, *x*, *y*, *z*, the change in temperature *ΔT*, and the elastic and thermal constants of the material. When the theorem of minimum total potential energy is enacted:

$$\delta W = 0 = \left(\frac{\delta W}{\delta a}\right)\delta a + \left(\frac{\delta W}{\delta b}\right)\delta b + \left(\frac{\delta W}{\delta a_1}\right)\delta a_1 + \left(\frac{\delta W}{\delta b_1}\right)\delta b_1 + \left(\frac{\delta W}{\delta a_2}\right)\delta a_2 + \left(\frac{\delta W}{\delta b_2}\right)\delta b_2 \quad (4.9)$$

A series of six nonlinear functions, in terms of six constants, was formulated. This problem can be solved numerically.

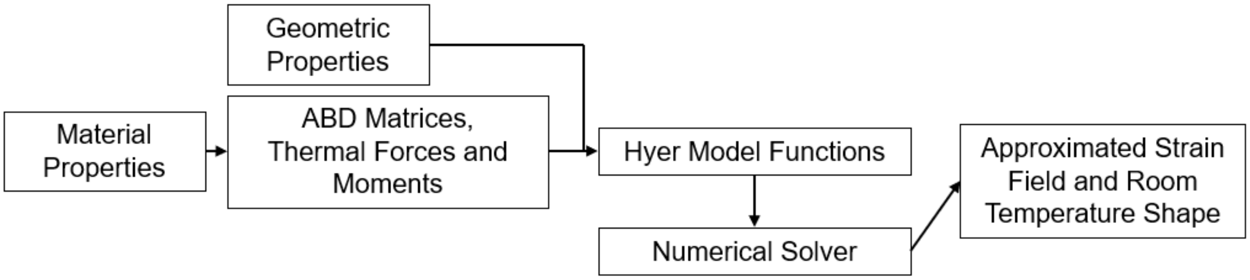

Figure 4.2 Flowchart figure of the analytical model.

The MATLAB code in the Appendix was created to facilitate this model. Using the laminate material, geometric, and thermal properties, the code first finds the *A*, *B*, and *D* matrices of the thermal forces and moments, using the material properties and the conventional classical lamination theory.

```
function [A,B,D,N,M] = ABDThermal(k,e1,e2,v12,g12,v21,thick,a1,a2,dt) ...
```

Figure 4.3 Function responsible for determining the *A*,*B*, and *D* matrices and thermal forces and moments.

These data are then used to formulate the six nonlinear equations of the model in terms of the six constants *a*, *b*, a_1, b_1, a_2, and b_2. These are solved using the MATLAB fsolve() function with a first guess of the constants, which can be used along with knowledge of the expected magnitudes and signs of *a* and *b* to solve the equations for the desired stable shape of the laminate, which is one of the two cylindrical shapes or the saddle shape. Typically, this study was concerned with comparing the curvatures of only one of the two cylinder shapes between different samples; the function variable a(2), which is *b*, can be set to zero in all instances where it shows up in the six equations, ensuring that the solution is a particular cylindrical shape where $a > 0$ and $b = 0$. This proved to be slightly more accurate in predicting the actual shapes of the experimental samples in most cases.

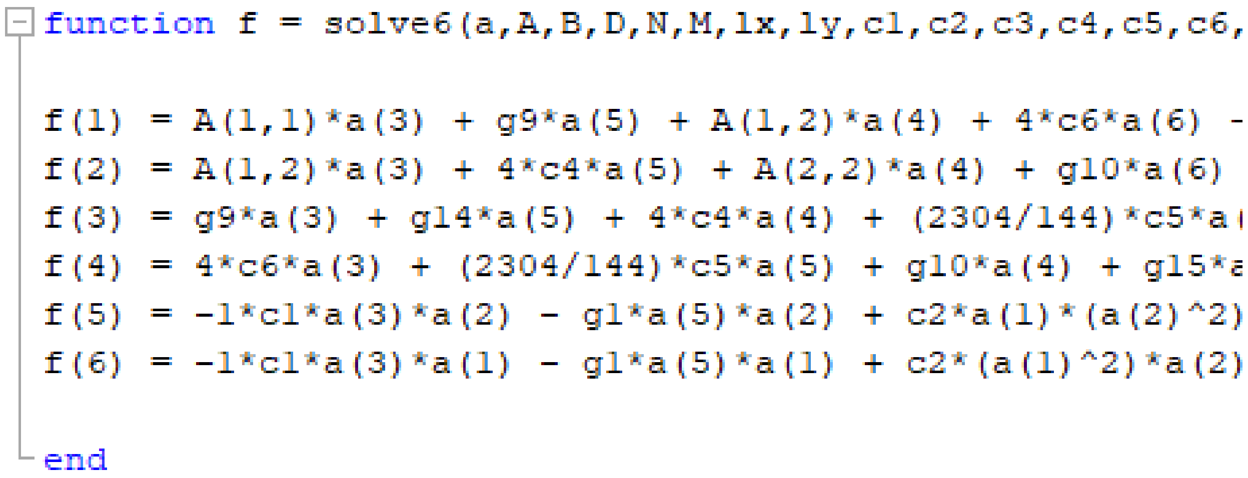

```
function f = solve6(a,A,B,D,N,M,lx,ly,c1,c2,c3,c4,c5,c6,

f(1) = A(1,1)*a(3) + g9*a(5) + A(1,2)*a(4) + 4*c6*a(6) -
f(2) = A(1,2)*a(3) + 4*c4*a(5) + A(2,2)*a(4) + g10*a(6)
f(3) = g9*a(3) + g14*a(5) + 4*c4*a(4) + (2304/144)*c5*a
f(4) = 4*c6*a(3) + (2304/144)*c5*a(5) + g10*a(4) + g15*
f(5) = -1*c1*a(3)*a(2) - g1*a(5)*a(2) + c2*a(1)*(a(2)^2)
f(6) = -1*c1*a(3)*a(1) - g1*a(5)*a(1) + c2*(a(1)^2)*a(2)

end
```

Figure 4.4 The series of functions in MATLAB code. a(i) represents the constants *a* and *b*.

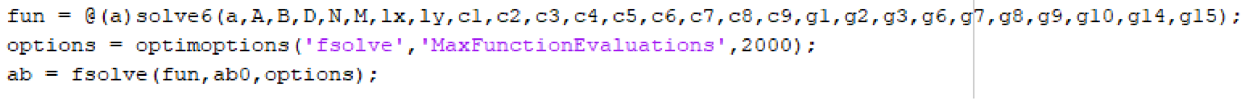

```
fun = @(a)solve6(a,A,B,D,N,M,lx,ly,c1,c2,c3,c4,c5,c6,c7,c8,c9,g1,g2,g3,g6,g7,g8,g9,g10,g14,g15);
options = optimoptions('fsolve','MaxFunctionEvaluations',2000);
ab = fsolve(fun,ab0,options);
```

Figure 4.5 The MATLAB code that solves the equations for the constants.

4.2 Finite Element Model

Finite Element Analysis (FEA) is another great tool for characterizing the properties of bistable laminates and has shown to be able to attain great accuracy in determining their room temperature shapes. FEA using ANSYS was explored for this reason, and the simple model that was created, although limited compared to FEA in other literature, proved to still be enlightening. The modeling process begins by using the ANSYS Composite Prep (ACP) module to mesh elements onto a plane of the desired laminate geometry. ACP also transforms the mesh into a composite laminate once the user specifies the plies in the desired layup. Subsequently, an ANSYS thermal module was used to simulate the curing conditions of the autoclave. The curing profile used for the autoclave experiments was mirrored in ANSYS using this module. The static structural module was then used to constrain the laminate in a manner consistent with autoclave vacuum bagging.

Subsequently, the ANSYS Composite Cure Simulation (ACCS) was added. ACCS is a proven tool that can accurately model resin shrinkage in laminates during the curing process owing to the gelation and subsequent cross-linking of the resin. To be able to analyze an accurate model for this study, it was decided to utilize the material properties found by Chava et al. [22] and model the material used in their study owing to a much higher percentage of properties being known for this material, leading to a much more complete model. However, the layup and number of plies remained consistent between the experiments and the model. These properties (Table 4.1) were used by the ACCS when convection was applied to the upper and lower surfaces of the simulated laminate, following the same cure cycle used in the experiments, which accurately mimicked the way that the laminate samples were heated during the autoclave experiments. ACCS then models the chemical changes within the laminate to determine the thermal shrinkage and warpage as well as the degree of cure. ACCS also virtually removes the boundary conditions to show an unconstrained room-temperature shape.

Table 4.1 List of material properties used by ACCS to model the material used for FEA study. Here, *x*, *y*, *z* are default global directions in the ACP model, which are converted into longitudinal and traverse fiber directions in ANSYS.

Material Property	**Value**	**Unit**
Density	1200	kg*m^3
Coefficients of Thermal Expansion *x*	0	1/°C
y	$3.82\text{x}10^{-5}$	1/°C
z	$3.82\text{x}10^{-5}$	1/°C
Young's Modulus *x*	$2.76\text{x}10^{11}$	Pa
y	$7.9\text{x}10^{9}$	Pa
z	$7.9\text{x}10^{9}$	Pa
Poisson's Ratio *xy*	0.35	
yz	0.45	
xz	0.35	
Shear Modulus *xy*	$5\text{x}10^{9}$	Pa
yz	$3.27\text{x}10^{9}$	Pa
xz	$5\text{x}10^{9}$	Pa
Cure Shrinkage *x*	0	1/mm
y	0.0073	1/mm
z	0.0073	1/mm
Fiber Volume Fraction	0.47	
Gelation Degree of Cure	0.2	

5 Results

The methods used in this study indicate that the properties of the laminates can be tracked throughout all stages of their processing, from the moment they begin curing to the final machining of the sample. For the application of bistable composites in structural aerospace components, this is a great boon, as changes that would have a relatively minor effect on symmetric laminates, such as changes in the residual strain due to curing, have a large effect on the geometry and snap through load of bistable laminates. This makes it crucial to understand how strain on the laminate develops throughout the process.

5.1 Digital Image Correlation Method for In-Situ Strain Results

The DIC system was utilized to track the e_{xx} strain over the course of the cure profile for three samples each of 15.24 cm by 15.24 cm, 15.24x10.16, 15.24x7.62, and 15.24x5.08 samples. The strains that develop in Figure 5.1 through 5.3 follow the temperature changes in the cure profile described in Section 3.1. In general, during the ramp phase of the curing cycle, the strain within the sample increased rapidly. Less so during the hold phases, and eventually the strains imposed by the thermal conditions level out as the degree of cure for the laminate becomes significant.

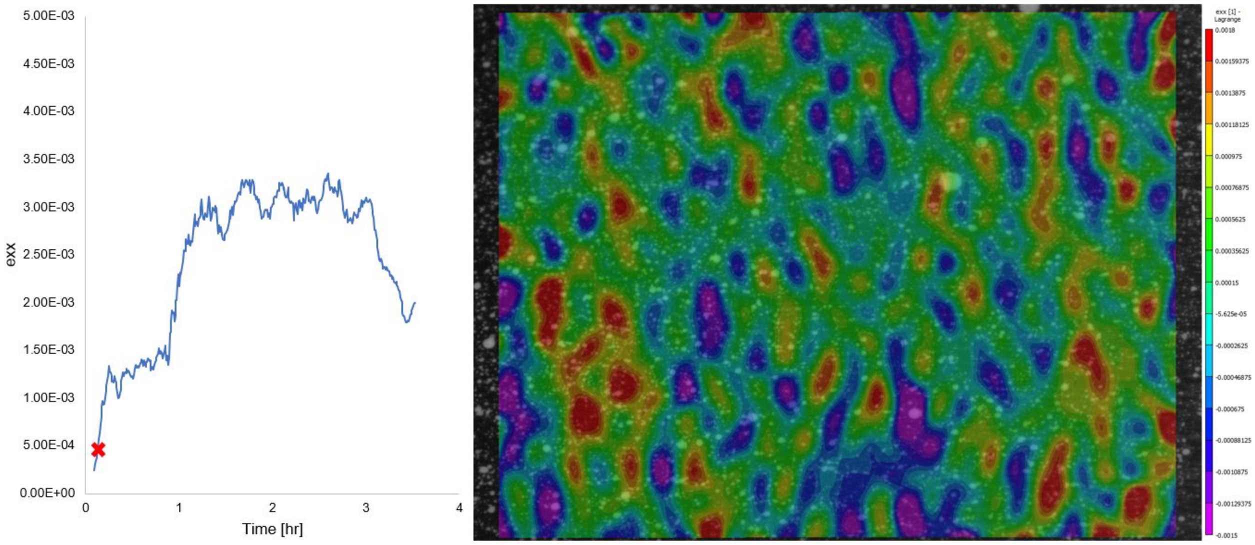

Figure 5.1 e_{xx} strains for 15.24 cm x 15.24 cm $[0_2/90_2]$ sample, ID 663. This is approximately 5 min into the cure cycle, and it can be seen from the random pattern and low strain magnitudes that almost no strain has yet developed in the laminate. Pictured area is approximately 6cm by 5cm.

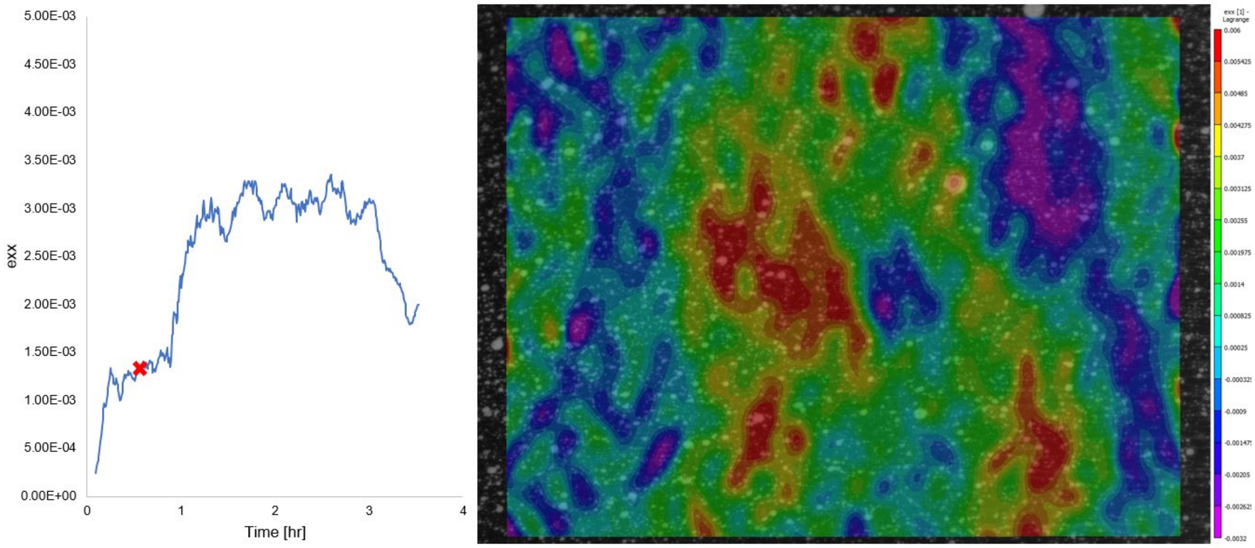

Figure 5.2 The e_{xx} strains for the same sample approximately 25 min into the curing cycle. On average, over the surface, a net positive e_{xx} strain is formed as its magnitude increases owing to thermal conditions.

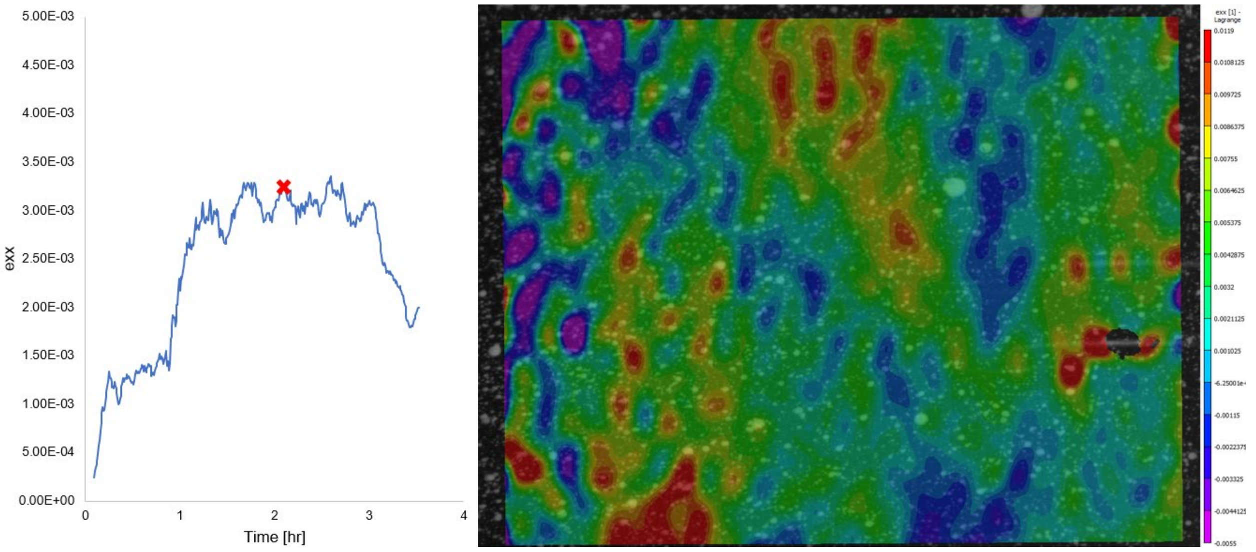

Figure 5.3 e_{xx} strains around 2 h into the cure, when the strain increase reached its peak and the contour plot became almost uniformly positive.

By comparing the e_{xx} strain profiles based on the dimensions of the samples, a pattern emerges. The 15.24x15.24 cm [6x6 in] samples exhibited the highest strain throughout, which was expected and correlated with the size of the sample having a higher curvature at room temperature. For this material and layup, the 15.24x7.62 cm [6x3 in] samples were bistable, whereas the 15.24x5.08 cm [6x2 in] samples were no longer stable. From literature, this is explained by one side of the sample becoming too short for bistability to occur, which means the so-called “critical length” of these samples is somewhere between 7.62 and 5.08 cm [2 and 3 inches]. In this context, one can create a theory as to why the strain throughout the cure cycle for the 15.24x10.16 cm [6x4] sample was much lower than that for the 15.24x15.24 cm samples, but there was far less decrease from 15.24x10.16 cm to 15.24x7.62 cm, and even less, if any, from 15.24x7.62 cm to 15.24x5.08 cm. This is evident in the change in the level of bistability behavior in the laminate. A square sample will have the maximum level of bistability compared to any sample in which one side is shortened, and as the length of one side decreases, the bistability decreases rapidly. This was also observed in the snap-through load test results. This means that in situations where a lower residual strain (which is correlated with higher laminate strength) is important, shortening one side of a square laminate would have little impact on its curvature geometry but has a relatively large effect on lowering the strain.

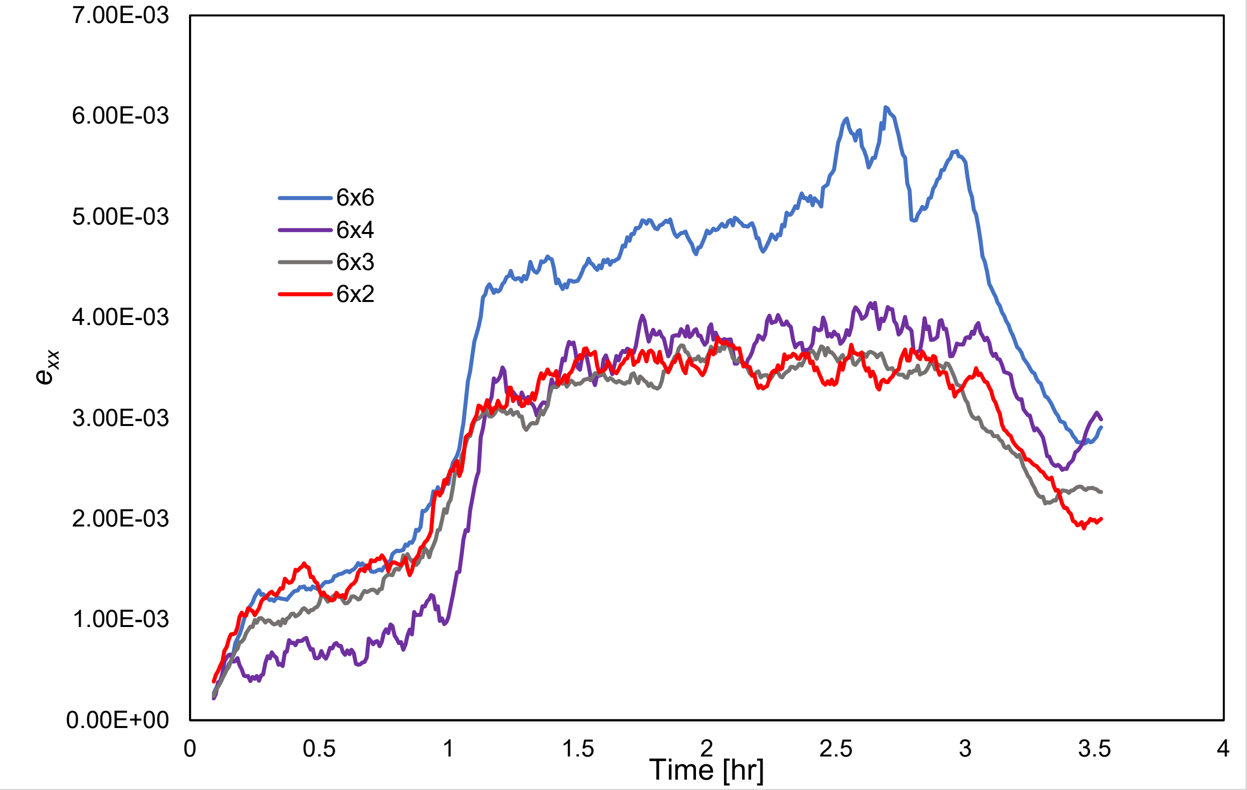

Figure 5.4 e_{xx} residual strains for multiple sizes of $[0_2/90_2]$ sample.

5.2 Curvature Measurements of Cured Samples Results

Curvature measurements of the autoclave samples were performed using the method outlined in Section 3.1. From Figure 5.5, a linear decrease in curvature corresponds to a decrease in the side length on the same axis. This is caused by the decreasing laminate residual strain easing, meaning less moment from the plies to force the laminate to assume a cylindrical shape and slowly revert to a saddle shape when the critical length is passed in the 15.24x5.08 cm [6x2 in] sample. Curvature is one of the most important parameters for potential morphing applications of bistable laminates.

Without the desired curvature, the structure will simply not be able to perform its function as a control surface or other components. To make the most efficient use of bistable laminates in terms of curvature performance, these results indicate that designers should use square sections of bistable laminates.

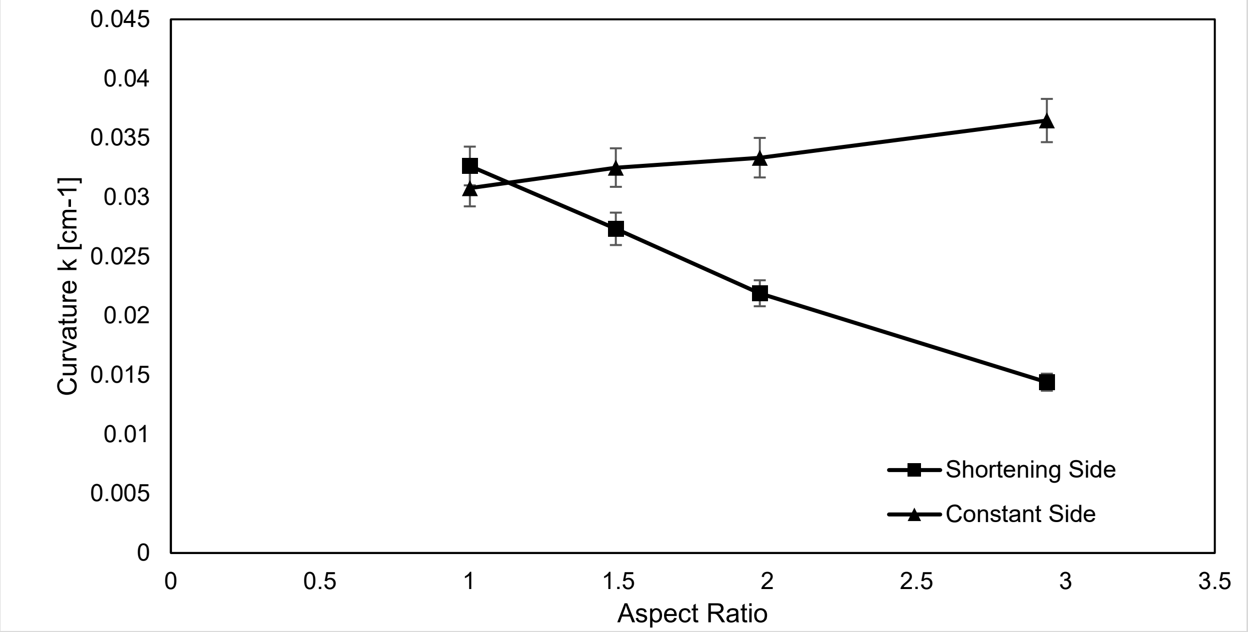

Figure 5.5 AR vs. curvature for [$0_2/90_2$] samples. The side that is 15.24 cm [6 in] for all samples stays mostly constant in curvature, unaffected by the decrease in length of the other side.

5.3 Effects of Post-Cure Machining

Depending on the situation, CFRP laminates can be almost entirely ready for use in a structure immediately after curing; however, further machining post-curing is often required. This could be due to cost-saving opportunities of being able to fashion multiple parts out of a single plate of CFRP instead of having to cure each individually, or it may not be possible to lay up a part with an irregular shape using pre-preg plies before curing. Water-jet cutters are excellent tools for machining CFRP laminates. They create clean, straight cuts, and the settings can be specified before cutting to prevent delamination. In this study, post-cure machining was simulated by creating smaller samples by two different methods. The first method was to lay up samples of these dimensions and cure them. The second method was to cut one side of the 15.24x7.62 cm samples to create smaller sizes. Then, the curvatures and snap-through loads of each (15.24x7.62 cm from autoclave and 15.24x7.62 cm made from cutting a 15.24x15.24 cm sample, for example) can be compared. The results in Figure 5.6 and Figure 5.7 indicate that the snap-through loads of laminate samples that have been cut to size using the water jet cutter require less force to snap through and have less curvature than identically sized samples that have not been machined. However, there is an inequality in the decrease in these parameters for the machined samples. Notably, on average, the snap-through load of the laminate decreased by 21%, whereas the curvatures of these samples only decreased by 7%. It is thought that the reason for this is that machining relaxes the residual stresses within the laminate. During curing, it is reasonable to assume that the edges of the laminate take on the most strain, and for this reason, when the laminate edge is machined off, the stress concentrated in the edges is removed, meaning that much less force is required to snap-through the laminate. It is also reasonable to assume that the high stress around the edges has more of an effect on snap-though action rather than over all curvature, as near the edge there is less lever arm for the stress there to bend the laminate, which would account for the difference in the curvature and snap-through load decrease. It should also be noted that the general trend for the snap-through loads is what was expected from the DIC strain results; as one side length decreases, there is a sharp fall in both residual strain and snap-through load immediately upon the sample geometry being changed from a square.

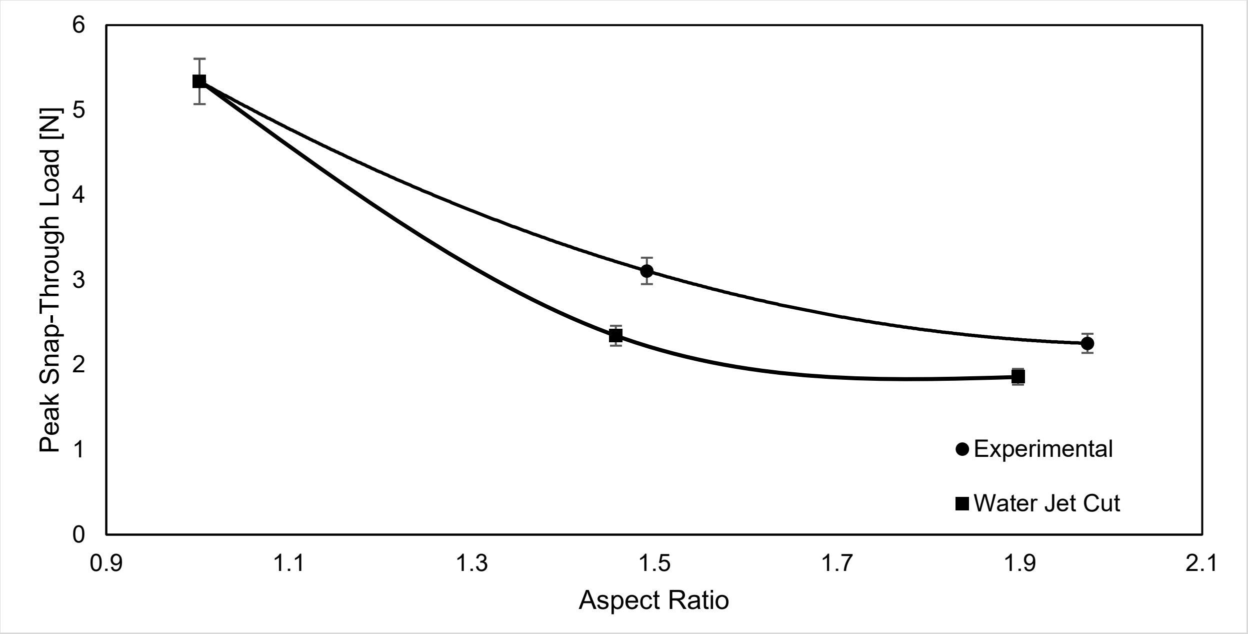

Figure 5.6 AR vs. snap-through load for machined and non-machined [$0_2/90_2$] samples.

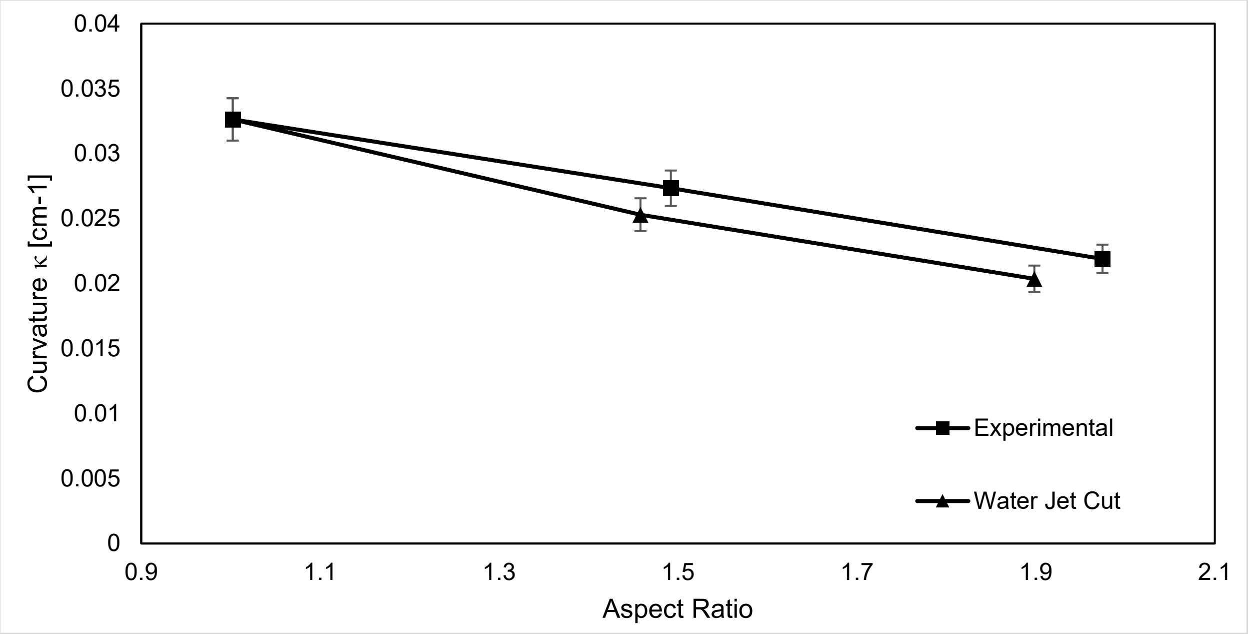

Figure 5.7 AR vs. curvature for the side of changing length for machined and non-machined [$0_2/90_2$] samples.

5.4 Effects of Cure Cycle Modification

To study the effects of drastically modifying the cure cycle on bistable laminates, it was decided to try an “interrupted” cure cycle that was previously shown to decrease residual strains within CFRP laminates [17]. However, as shown in Figure 5.8, the curing cycle had an opposite effect on the laminates. This is most likely because the cure profile in this study, which lacks a dwell section before heating to the cure temperature, is different from the cure cycle used in the experiments in this research. For the experiments exploring this curing cycle, the laminate was removed from the autoclave immediately upon first reaching the curing temperature, as was done in Chava et al.’s paper [19]. This was done to allow the laminate to begin curing at low, near ambient temperature, but due to the difference in the cure profile, this may not have had the same effect on the samples in this study as it did in the Sandeep et al. experiments. However, upon reheating, the residual strains of the samples were significantly higher. Nevertheless, this was still deemed to be valuable to the study as proof of cure cycle modification having a significant effect on the curvature of bistable laminates. This cure profile change resulted in a 66% increase in curvature of 15.24×15.24 cm [6x6 in] samples. Although conventionally, increasing the residual strain within a laminate is thought to be detrimental, in the case of bistable laminates, it could be advantageous for applications as not only could the increase in curvature be beneficial in morphing applications, but also by raising the residual strain within smaller samples such as the 15.24x5.08 cm [6x2 in], which are normally not large enough to be bistable, could allow these smaller parts to exhibit bistable behavior and potentially be useful in applications that require the size of parts to be small, such as in compact drone aircraft. In short, cure profile modification can drastically effect the curvature of the laminate independent of the laminate geometry, which is a significant advantage.

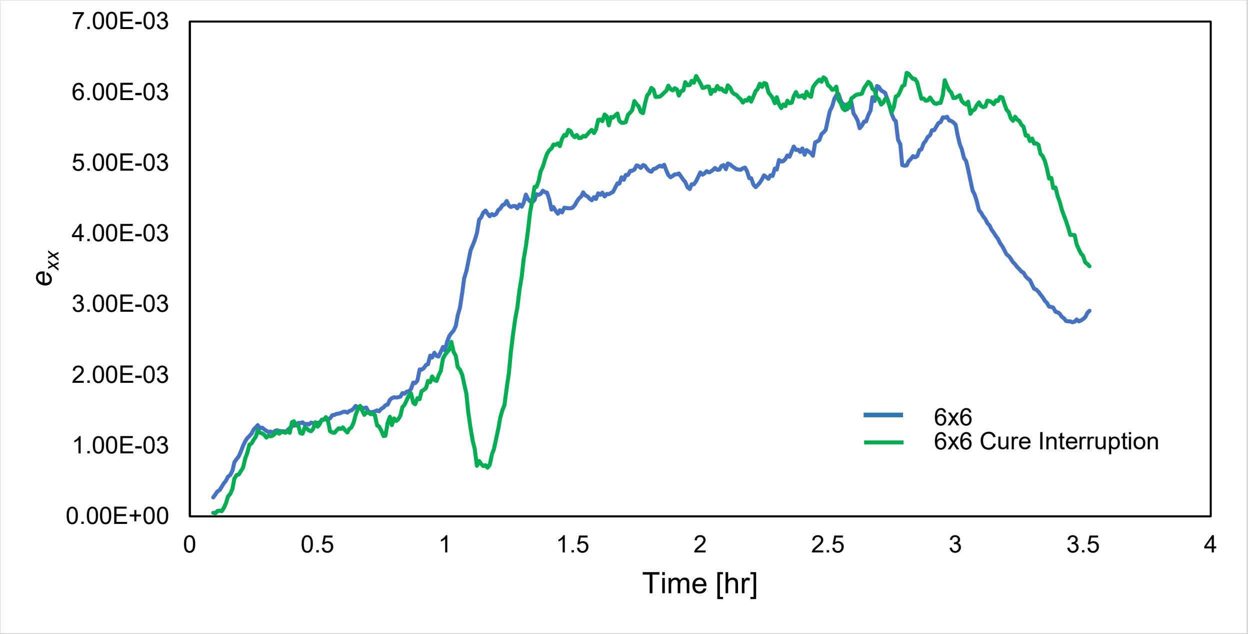

Figure 5.8 e_{xx} residual strains for $[0_2/90_2]$ 15.24×15.24 cm [6x6 in] samples with and without cure interruption.

5.5 Analytical Model

The analytical model adapted from Hyer's [2] paper allows the experiments in this study to be verified against accepted theory. The results (Figure 5.9) show that the curvature of the samples closely follows that predicted by the model. Although it has been reported in the literature that FEA models more closely follow the true shape of bistable laminates, this proves that analytic models are an acceptable and computationally inexpensive way of predicting the overall curvatures of real-life laminates, which is likely sufficient for most applications. One disadvantage is that unlike FEA models, analytical models cannot be used to predict snap-through loads.

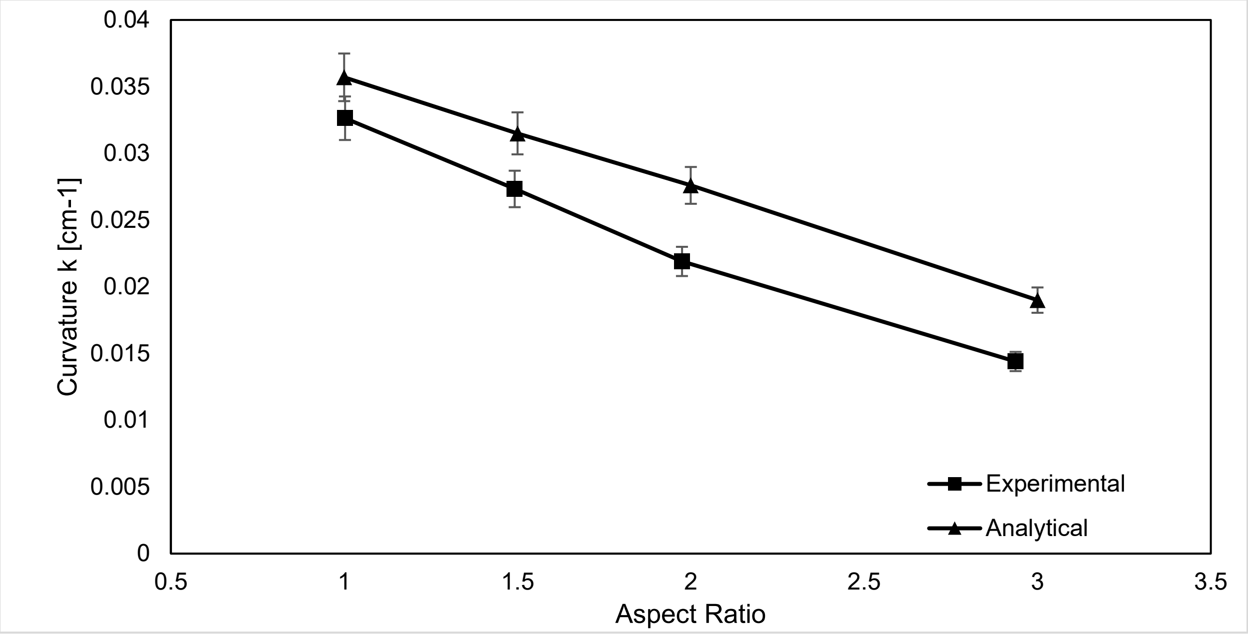

Figure 5.9 Aspect ratio vs. curvature for the side of changing length for the experimental $[0_2/90_2]$ samples and from the analytical model.

5.6 ANSYS Cure Simulation

The model created in ANSYS for this study using the results from the ACCS cure simulator is limited in scope compared to ABAQUS and ANSYS models in literature as there was difficulty with getting ANSYS to model the correct room temperature shapes. Despite the best efforts, the ANSYS model only predicted the saddle shape, which is predicted by CLT, even when forces and moments were applied to the laminate after the curing simulation. However, upon analyzing the curvatures for the saddle shapes (Figure 5.10), they followed the same trend as the experimental samples and the analytical model, although the magnitudes of the curvatures did not match because of the difference in cylindrical and saddle shapes.

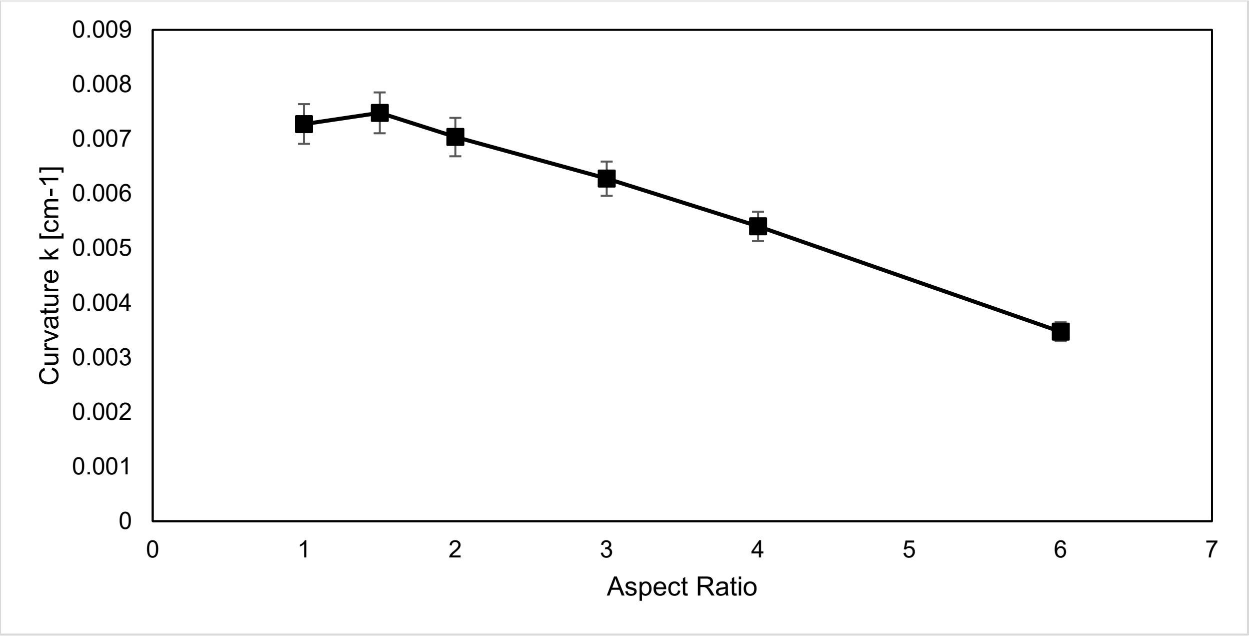

Figure 5.10 Aspect ratio vs. curvature for the side of changing length from the ANSYS FEA model.

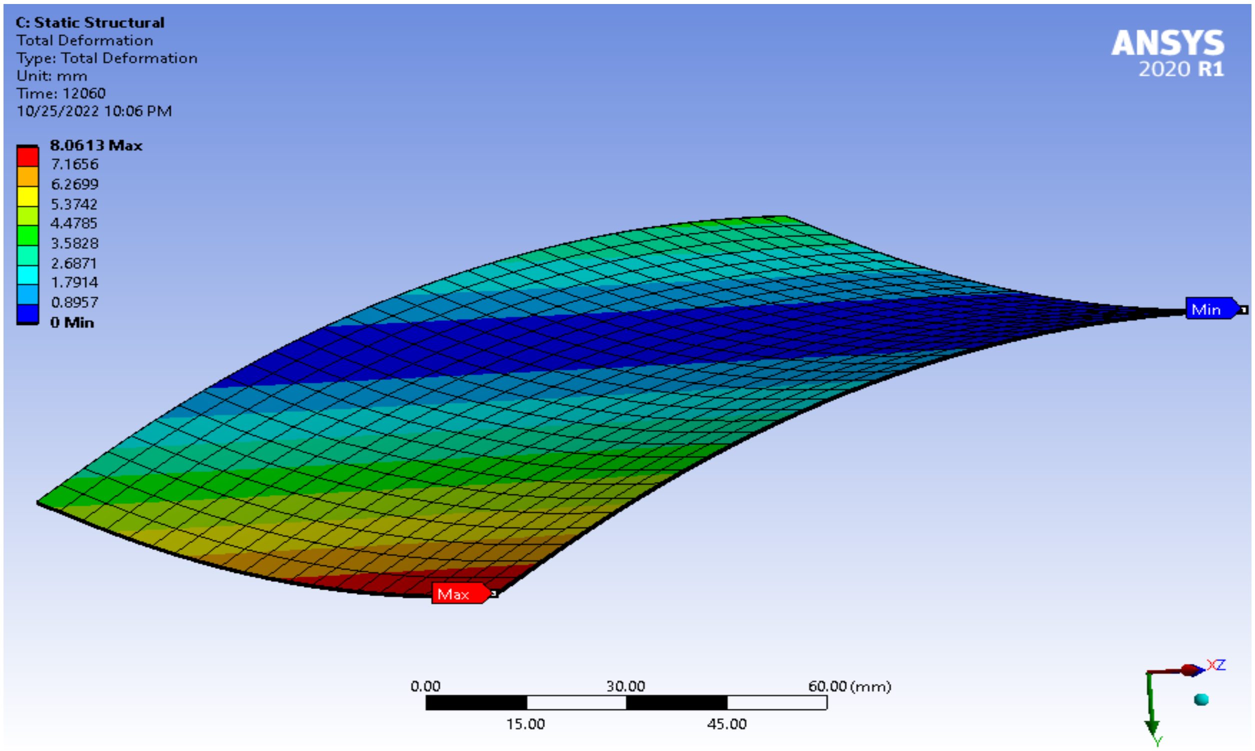

Figure 5.11 Saddle shaped laminate in ANSYS.

6 Discussion

6.1 Comparison of Results from Literature

Tawfik et al. [11] is a good place to start for a direct comparison of results from this study to that of another paper. Figure 9 of the paper [11] shows that the relationship between laminate AR and snap-through load is reproducible between their experiments and the FEA model using ABAQUS and the snap-through load experiments in this study. Because of either the material difference or a difference in laminate size, their plot can extend the results to an AR of 6, showing that as the AR increases further, the decrease in snap-through load becomes less significant, a trend that is expected to be seen based on the plots of e_{xx} in this study. They also noted a percent difference in experimental curvature calculations compared to Hyer's model of 19.5% and 28.0% for two different samples. This is very similar to the average percent difference calculated between the experimental and analytical curvature data in this study (20.7 %), even though the method of approximating curvatures between the two studies is slightly different.

Using the plots of the nondimensional force response from Phatak et al. [10] in Figures 18 and 20, we can compare the force results in this study with the FEA model and their experiments. Using their formulae, one can find that for the 15.24×15.24 cm [6x6 in] sample in this study, $F/E_1*L^2 = 1.77x10^{-9}$ and $L/t = 254$. This is significantly different from the expected curve from the FEA results but is closer to the other experimental results, although not by much. This could be due to the difference in constraint between the load tests performed in this study and in Phatak et al.'s paper, where the sides are constrained at the center instead of having all edges free, as in this study and the paper of Tawfik et al.

6.2 Discussion on the Analytical Model

The analytical model used in this study was adjusted several times to increase its accuracy. To improve the correlation with the experimental samples, it was adjusted only to find solutions to the series of equations that resulted in $b = 0$. This was to ensure that a cylinder of a specific orientation was acquired from the model and to avoid solutions that had greater curvatures in y than was seen for real-world shapes. A comparison of the experimental and analytical models with b forced to be zero, and the unaltered model is shown in Figure 6.1. In both models, the initial guess for b in the solver is always set to zero; however, the solver overwhelmingly selects solutions that result in an unrealistically saddle-like shape if all instances of b in the equations are also set to zero, forcing pure cylindrical shapes.

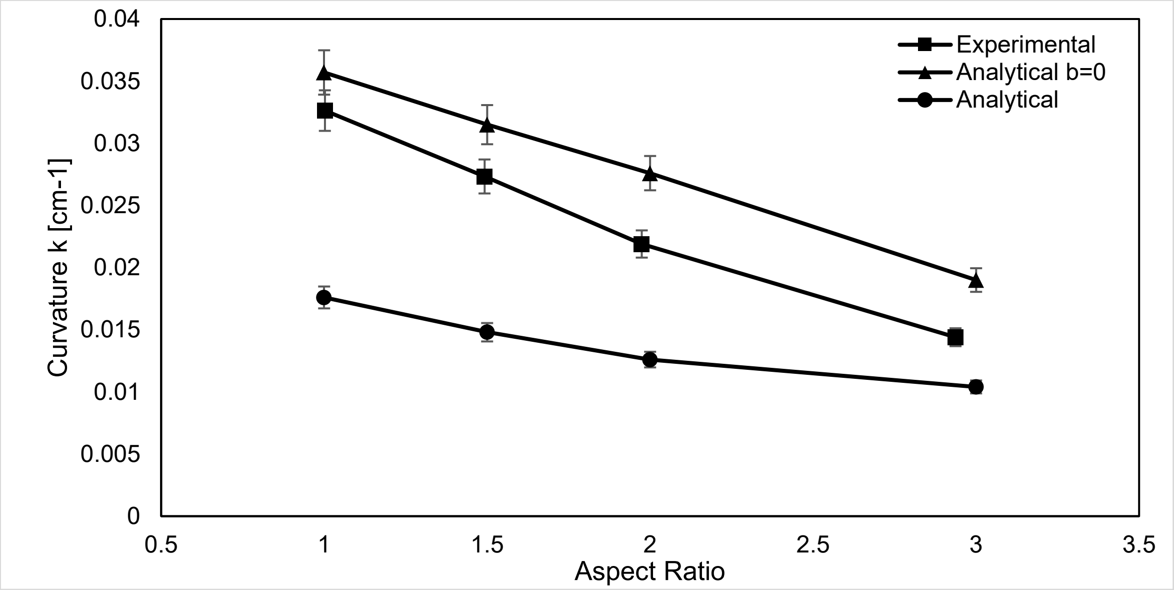

Figure 6.1 Experimental curvature results for the shortening side compared to the version of the analytical model where only solutions where b=0 are allowed and the model without that restriction.

7 Conclusions and Future Work

Through the course of this research, many insights were gained that clarify the questions that designers of aerospace applications have surrounding bistable laminates. Through the analysis of the laminates throughout the cure cycle with DIC, the full picture of strain development in bistable laminates can be clearly seen, both with conventional and modified cure cycles, such as interrupted curing. Combined with the results from snap-through load testing, the important role of laminate geometry can be more clearly understood, and along with modifying the cure cycle, designers can use the insights from this novel analysis to improve the efficiency of their bistable structures, adding much needed depth to the design space. Through this research, the effects of post-cure machining with water-jet cutters can be better understood, and it is shown that this type of machining decreases the snap-through load and curvature of the laminates. This will allow designers to have tools to both increase and decrease the snap-through loads and curvatures of bistable laminates, which would be extremely helpful when fabricating parts for morphing aerospace components. A robust analytical model was adapted into MATLAB and modified to allow quick analysis of bistable laminate curvatures.

7.1 Future Work

There is still work to be done before bistable laminates can find their place in the aerospace industry. In particular, one very important topic that has so far been neglected is fatigue response. There has been very little research on fatigue in bistable laminates, but it is paramount to determine whether there will be a change in behavior or a heightened risk of failure for bistable components that often snap between two stable states. There are also more questions that can be answered about post-cure machining, such as studying how adding common features, such as fastener holes or cut-out sections, affects laminate performance, as well as studying alternative methods of machining other than water jet cutters and how they compare. Finally, continuing work for morphing applications and perhaps even demonstrative vehicles that apply bistable laminates and comparing the performance of these vehicles that employ morphing laminates versus those that use conventional methods would show the potential weight savings and efficiency increases of this technology in a very real way, encouraging further research.

8 REFERENCES

[1] Brian Dunbar. (2003, June 12). NASA - Designing the 21st Century Aerospace Vehicle. National Aeronautics and Space Administration. Retrieved April 21, 2023, from https://www.nasa.gov/vision/earth/improvingflight/morphing.html

[2] Hyer, M. W. (1982). The room-temperature shapes of four-layer unsymmetric cross-ply laminates. Journal of Composite Materials, 16(4), 318-340.

[3] Daniel, I. M., Ishai, O., Daniel, I. M., & Daniel, I. (2006). Engineering mechanics of composite materials (Vol. 1994). New York: Oxford university press.

[4] Bowen, C. R., Butler, R., Jervis, R., Kim, H. A., & Salo, A. I. T. (2007). Morphing and shape control using unsymmetrical composites. Journal of Intelligent Material Systems and Structures, 18(1), 89-98.

[5] Mattioni, F., Weaver, P. M., Potter, K. D., & Friswell, M. I. (2008, April). The application of thermally induced multistable composites to morphing aircraft structures. In Industrial and Commercial Applications of Smart Structures Technologies 2008 (Vol. 6930, p. 693012). International Society for Optics and Photonics.

[6] Scarselli, G., Nicassio, F., Pinto, F., Ciampa, F., Iervolino, O., & Meo, M. (2016). A novel bistable energy harvesting concept. Smart Materials and Structures, 25(5), 055001.

[7] Zhang, Z., Wu, H., He, X., Wu, H., Bao, Y., & Chai, G. (2013). The bistable behaviors of carbon-fiber/epoxy anti-symmetric composite shells. Composites Part B: Engineering, 47, 190-199.

[8] Dano, M. L., & Hyer, M. W. (1998). Thermally-induced deformation behavior of unsymmetric laminates. International journal of solids and structures, 35(17), 2101-2120.

[9] Zhang, Z., Wu, H., Ye, G., Wu, H., He, X., & Chai, G. (2014). Systematic experimental and numerical study of bistable snap processes for anti-symmetric cylindrical shells. Composite Structures, 112, 368-377.

[10] Phatak, S., Myers, O. J., Li, S., & Fadel, G. (2021). Defining relationships between geometry and behavior of bistable composite laminates. Journal of Composite Materials, 55(22), 3049-3059.

[11] Tawfik, S., Tan, X., Ozbay, S., & Armanios, E. (2007). Anticlastic stability modeling for cross-ply composites. Journal of composite materials, 41(11), 1325-1338.

[12] Giddings, P. F., Bowen, C. R., Salo, A. I., Kim, H. A., & Ive, A. (2010). Bistable composite laminates: effects of laminate composition on cured shape and response to thermal load. Composite Structures, 92(9), 2220-2225.

[13] Mattioni, F., Weaver, P. M., & Friswell, M. I. (2009). Multistable composite plates with piecewise variation of lay-up in the planform. International Journal of Solids and Structures, 46(1), 151-164.

[14] Betts, D. N., Salo, A. I., Bowen, C. R., & Kim, H. A. (2010). Characterisation and modelling of the cured shapes of arbitrary layup bistable composite laminates. Composite Structures, 92(7), 1694-1700.

[15] Zhang, Z., Pei, K., Sun, M., Wu, H., Wu, H., Jiang, S., & Zhang, F. (2022). Tessellated multistable structures integrated with new transition elements and antisymmetric laminates. Thin-Walled Structures, 170, 108560.

[16] Anilkumar, P. M., Haldar, A., Scheffler, S., Jansen, E. L., Rao, B. N., & Rolfes, R. (2022). Morphing of bistable variable stiffness composites using distributed MFC actuators. Composite Structures, 289, 115396.

[17] Liu, Y., Zhang, J., Pan, D., Wu, Z., & Wang, Q. (2023). Resonant actuation based on dynamic characteristics of bistable laminates. Machines, 11(3), 318.

[18] Rogan, B. (2021). The Effect of Part Curvature on the Formation of Residual Stresses in Carbon Fiber Prepreg Laminates.

[19] Chava, S., Namilae, S., & Al-Haik, M. (2022). Residual stress reduction during composite manufacturing through cure modification: In situ analysis. Journal of Composite Materials, 56(6), 975-988.

[20] Cowley, K. D., & Beaumont, P. W. (1997). The measurement and prediction of residual stresses in carbon-fibre/polymer composites. Composites Science and Technology, 57(11), 1445-1455.

[21] MAXIEM 1515 Abrasive Waterjet | OMAX Waterjet. (n.d.). OMAX Waterjet. https://www.omax.com/en/us/maxiem-waterjet/1515

[21] Chava, S. (2021). Kinematics of Inter-Ply Interfaces In Composite Manufacturing.

9 APPENDIX A: Hyer Model Code, MATLAB

```matlab
%Code for Hyer's Model MATLAB
%Written by Evan Medora
clear all;
close all;
clc;
cla;

lx = (1)*(152.4/1000);
ly = (1)*(152.4/1000);
ab0 = [200,0,0,0,0,0];

p1 = 'How many layers? ';
k = input(p1);
e1 = 130e9;
e2 = 12e9;
v12 = 0.35;
g12 = 4.8e9;
v21 = (v12/e1)*e2;
thick = 0.6/1000;
a1 = -0.106e-6;
a2 = 25.6e-6;
dt = -110;
[x,y] = meshgrid(-(lx/2):0.0001:(lx/2),-(ly/2):0.0001:(ly/2));
sx = size(x);
sy = size(y);

[A,B,D,N,M] = ABDThermal(k,e1,e2,v12,g12,v21,thick,a1,a2,dt);

c1 = (A(1,1)*(ly^2))/48;
c2 = (A(1,1)*(ly^4))/1280;
c3 = (B(1,1)*(ly^2))/48;
c4 = (A(1,2)*(lx^2))/48;
c5 = (A(1,2)*(lx^2)*(ly^2))/2304;
c6 = (A(1,2)*(ly^2))/48;
c7 = (A(2,2)*(lx^2))/48;
c8 = (A(2,2)*(lx^4))/1280;
c9 = (B(2,2)*(lx^2))/48;
g1 = (A(1,1)*(lx^2)*(ly^2))/576;
g2 = (B(1,1)*(lx^2))/12;
g3 = (A(1,2)*(ly^4))/320;
g6 = (A(1,2)*(lx^4))/328;
g7 = (A(2,2)*(lx^2)*(ly^2))/576;
g8 = (B(2,2)*(ly^2))/12;
g9 = (A(1,1)*(lx^2))/12;
g10 = (A(2,2)*(ly^2))/12;
g14 = (A(1,1)*(lx^4))/80;
g15 = (A(2,2)*(ly^4))/80;

fun = @(a)solve6(a,A,B,D,N,M,lx,ly,c1,c2,c3,c4,c5,c6,c7,c8,c9,g1,g2,g3,g6,g7,g8,g9,g10,g14,g15);
```

```
options = optimoptions('fsolve','MaxFunctionEvaluations',2000);
ab = fsolve(fun,ab0,options);

a = ab(1,1);
b = ab(1,2);
w = (1/2).*((a.*(x.^2))+(b.*(y.^2)));

surf(x,y,w,'EdgeColor','none')
axis equal
hold on
plot3([0 0.05],[0 0],[0 0],'Color','red','LineWidth',3)
plot3([0 0],[0 0.05],[0 0],'Color','green','LineWidth',3)
plot3([0 0],[0 0],[0 0.05],'Color','blue','LineWidth',3)

chx = 100*abs(w(1,(sx(2)+1)/2) - ((w(1,1)+w(1,end))/2));
chy = 100*abs(w((sy(2)+1)/2,1) - ((w(1,1)+w(end,1))/2));
cfx = @(R) (chx^2) - 2*chx*R + (R^2)*(sin((lx*50)/R))^2;
cfy = @(R) (chy^2) - 2*chy*R + (R^2)*(sin((ly*50)/R))^2;
R0 = 100;
radiusx = fzero(cfx,R0);
radiusy = fzero(cfy,R0);
curvaturex = 1/radiusx;
curvaturey = 1/radiusy;
disp('Curvature X [cm-1]:')
disp(curvaturex)
disp('Curvature Y [cm-1]:')
disp(curvaturey)

function [A,B,D,N,M] = ABDThermal(k,e1,e2,v12,g12,v21,thick,a1,a2,dt)

p2 = 'Layer fiber orientation? ';

th = zeros(k,1);
t = zeros(k,1);
ax = zeros(k,1);
ay = zeros(k,1);
as = zeros(k,1);
m = zeros(k,1);
n = zeros(k,1);
zk = zeros(k,1);
q11 = zeros(k,1);
q22 = zeros(k,1);
q12 = zeros(k,1);
q66 = zeros(k,1);
T11 = zeros(k,1);
T12 = zeros(k,1);
T13 = zeros(k,1);
T21 = zeros(k,1);
T22 = zeros(k,1);
T23 = zeros(k,1);
T31 = zeros(k,1);
T32 = zeros(k,1);
```

```
T33 = zeros(k,1);
qxy = cell(k,1);

ht1 = zeros(k,1);
ht2 = zeros(k,1);
htx = zeros(k,1);
hty = zeros(k,1);
hts = zeros(k,1);
htxy = cell(k,1);
Qet = zeros(3,1);
Qezt = zeros(3,1);
N = zeros(3,1);
M = zeros(3,1);

for i = 1:k
    disp('Layer number: ')
    disp(i)

    ht1(i,1) = dt*a1;
    ht2(i,1) = dt*a2;

    th(i,1) = input(p2);
    t(i,1) = thick;
    m(i,1) = cosd(th(i,1));
    n(i,1) = sind(th(i,1));

    q11(i,1) = (e1/(1 - v12*v21));
    q22(i,1) = (e2/(1 - v12*v21));
    q12(i,1) = ((e1*v21)/(1 - v12*v21));
    q66(i,1) = g12;

    T11(i,1) = (m(i,1)^2);
    T12(i,1) = (n(i,1)^2);
    T13(i,1) = 2*m(i,1)*n(i,1);
    T21(i,1) = (n(i,1)^2);
    T22(i,1) = (m(i,1)^2);
    T23(i,1) = -2*m(i,1)*n(i,1);
    T31(i,1) = -1*m(i,1)*n(i,1);
    T32(i,1) = m(i,1)*n(i,1);
    T33(i,1) = ((m(i,1)^2)-(n(i,1)^2));

    qxy{i,1} = inv([T11(i,1), T12(i,1), T13(i,1); T21(i,1), T22(i,1), T23(i,1); T31(i,1),
T32(i,1), T33(i,1);])*[q11(i,1), q12(i,1), 0; q12(i,1), q22(i,1), 0; 0, 0, 2*q66(i,1)]*[T11(i,1),
T12(i,1), T13(i,1); T21(i,1), T22(i,1), T23(i,1); T31(i,1), T32(i,1), T33(i,1);];
    qxy{i,1}(:,3) = 0.5*(qxy{i,1}(:,3));

    htx(i,1) = ht1(i,1)*(m(i,1)^2) + ht2(i,1)*(n(i,1)^2);
    hty(i,1) = ht1(i,1)*(n(i,1)^2) + ht2(i,1)*(m(i,1)^2);
    hts(i,1) = 2*(ht1(i,1) - ht2(i,1))*m(i,1)*n(i,1);
    ax(i,1) = htx(i,1)/dt;
    ay(i,1) = hty(i,1)/dt;
    as(i,1) = hts(i,1)/dt;
```

```
    htxy{i,1} = [htx(i,1); hty(i,1); hts(i,1);];
end
z0 = (-0.5*sum(t, 'all'));
for i2 = 1:k
    if i2 == 1
        zk(i2,1) = z0 + t(i2,1);
    else
        zk(i2,1) = t(i2,1) + zk(i2-1,1);
    end
end

A = zeros(3,3);
B = zeros(3,3);
D = zeros(3,3);
for i3 = 1:k
   if i3 == 1
       A = A + qxy{i3,1}*(zk(i3,1) - z0);
       B = B + 0.5*qxy{i3,1}*(((zk(i3,1))^2) - (z0^2));
       D = D + (1/3)*qxy{i3,1}*(((zk(i3,1))^3) - (z0^3));

       Qet = (qxy{i3,1}*htxy{i3,1})*t(i3,1);
       N = N + Qet;
       Qezt = (qxy{i3,1}*htxy{i3,1})*(0.5*(zk(i3,1) + z0))*t(i3,1);
       M = M + Qezt;
   else
       A = A + qxy{i3,1}*(zk(i3,1) - zk(i3-1,1));
       B = B + 0.5*qxy{i3,1}*(((zk(i3,1))^2) - ((zk(i3-1,1))^2));
       D = D + (1/3)*qxy{i3,1}*(((zk(i3,1))^3) - ((zk(i3-1,1))^3));

       Qet = (qxy{i3,1}*htxy{i3,1})*t(i3,1);
       N = N + Qet;
       Qezt = (qxy{i3,1}*htxy{i3,1})*(0.5*(zk(i3,1) + zk(i3-1,1)))*t(i3,1);
       M = M + Qezt;
   end
end

end

function f =
solve6(a,A,B,D,N,M,lx,ly,c1,c2,c3,c4,c5,c6,c7,c8,c9,g1,g2,g3,g6,g7,g8,g9,g10,g14,g15)

f(1) = A(1,1)*a(3) + g9*a(5) + A(1,2)*a(4) + 4*c6*a(6) - N(1,1) - c1*a(1)*a(2) - B(1,1)*a(1) -
c4*a(1)*a(2);
f(2) = A(1,2)*a(3) + 4*c4*a(5) + A(2,2)*a(4) + g10*a(6) - N(2,1) - c6*a(1)*a(2) - c7*a(1)*a(2) -
B(2,2)*a(2);
f(3) = g9*a(3) + g14*a(5) + 4*c4*a(4) + (2304/144)*c5*a(6) - N(1,1)*((lx^2)/2) - g1*a(1)*a(2) -
g2*a(1) - g6*a(1)*a(2);
f(4) = 4*c6*a(3) + (2304/144)*c5*a(5) + g10*a(4) + g15*a(6) - N(2,1)*((ly^2)/2) - g3*a(1)*a(2) -
g7*a(1)*a(2) - g8*a(2);
f(5) = -1*c1*a(3)*a(2) - g1*a(5)*a(2) + c2*a(1)*(a(2)^2) + c3*a(1)*a(2) - B(1,1)*a(3) - g2*a(5) +
c3*a(1)*a(2) + D(1,1)*a(1) - c6*a(4)*a(2) - g3*a(6)*a(2) + c5*a(1)*(a(2)^2) + D(1,2)*a(2) -
c4*a(3)*a(2) - g6*a(5)*a(2) + c5*a(1)*(a(2)^2) - g7*a(4)*a(2) -g7*a(6)*a(2) + c8*a(1)*(a(2)^2) +
```

```
c9*(a(2)^2) + (N(1,1)*((ly^2)/48))*a(2) + (N(2,1)*((lx^2)/48))*a(2) + M(1,1);
f(6) = -1*c1*a(3)*a(1) - g1*a(5)*a(1) + c2*(a(1)^2)*a(2) + c3*(a(1)^2) - c6*a(1)*a(4) -
g3*a(1)*a(6) + c5*(a(1)^2)*a(2) - c4*a(3)*a(1) - g6*a(5)*a(1) + c5*(a(1)^2)*a(2) + D(1,2)*a(1) -
c7*a(4)*a(1) - g7*a(6)*a(1) + c8*(a(1)^2)*a(2) + c9*a(1)*a(2) - B(2,2)*a(4) - g8*a(6) +
c9*a(1)*a(2) + D(2,2)*a(2) + (N(1,1)*((ly^2)/48))*a(1) + (N(2,1)*((lx^2)/48))*a(1) + M(2,1);
end
```